

**STUDY OF THE THERMOMAGNETIC PROPERTIES OF ALNICO V
MAGNETIC RIBBON.**

SUBMITTED

BY

Md. Mahamudul Hasan

Roll No.1014142515F

Session: October, 2014

*A Dissertation Submitted to the Department of Physics, Bangladesh University of
Engineering and Technology (BUET) in Partial Fulfillment of the Requirement
for the Degree of
MASTER OF SCIENCE (M.Sc) IN PHYSICS*



Department of Physics

**BANGLADESH UNIVERSITY OF ENGINEERING AND TECHNOLOGY
(BUET), DHAKA-1000, BANGLADESH**


**BANGLADESH UNIVERSITY OF ENGINEERING & TECHNOLOGY (BUET),
DHAKA
DEPARTMENT OF PHYSICS**

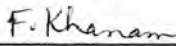



CERTIFICATION OF THESIS


The thesis titled “**STUDY OF THE THERMOMAGNETIC PROPERTIES OF ALNICO V MAGNETIC RIBBON**” submitted by **Md. Mahamudul Hasan**, Roll No: **1014142515F**, Session: **October/2014**, has been accepted as satisfactory in partial fulfillment of the requirement for the degree of **Master of Science (M.Sc.) in Physics** on **22 JANUARY 2017**.

BOARD OF EXAMINERS

1. 

Dr. Md. Feroz Alam Khan
Professor
Department of Physics, BUET, Dhaka
**Chairman
(Supervisor)**
2. 

Mrs. Fahima Khanam
Professor & Head
Department of Physics, BUET, Dhaka
**Member
(Ex-Officio)**
3. 

Dr. A.K.M. Akther Hossain
Professor
Department of Physics, BUET, Dhaka
Member
4. 

Dr. Ishtiaque M. Syed
Professor
Department of Physics, University of Dhaka
**Member
(External)**

CANDIDATE'S DECLARATION

It is hereby declared that this thesis or any part of it has not been submitted elsewhere for the award of any degree or diploma.

Md. MAHAMUDUL Hasan

(Md. Mahamudul Hasan)

Roll No. 1014142515F

Session: October 2014

Dedicated to
My beloved Parents and Teachers
Who inspired and influenced me in higher study

C O N T E N T S

CHAPTER 1	INTRODUCTION	1-6
1.1	Introduction	1
1.2	Purpose of Study	2
1.3	Objective	3
1.4	Outline line of this thesis	4
	References	6
CHAPTER 2	LITERATURE REVIEW	7-24
2.1	History of Alnico Alloys	7
2.2	Magnetic origin of Alnico Alloys	9
2.3	Manufacturing Process	14
2.4	Heat Treatment	14
2.5	Alloy Addition	17
2.6	Coercivity Enhancers	18
	References	24
CHAPTER 3	EXPERIMENTAL PROCEDURE	26-35
3.1	Arc Melting	26
3.2	Melt Spinning	27
3.3	Hysteresis Loop	28
3.4	4 X-ray Powder Diffraction	31
3.5	Scanning Electron Microscopy	32
3.6	Equipment needed for sample preparation and characterization.	33
	References	35
CHAPTER 4	SPINODAL DECOMPOSITION	
4.1	Introduction	38
4.2	The Mechanism of Spinodal Decomposition	39
4.3	The Evolution of Concentration Profiles	42
4.4	The Cahn-Hilliard Equation	44
4.5	Spinodial Decomposition vs. Nucleation and Growth	45
4.6	Coherency strains	46

4.7	Fourier transform	51
4.8	Dynamics in k-space	55
	References	57

CHAPTER 5 RESULTS AND DISCUSSIONS

5.1	Introduction	59
5.2	surface morphology of alnico v	60
5.3	Elemental analysis	63
5.4	X-ray Diffraction of meltspun Alnico V ribbon	65
5.5	Effect of mechanical alloying on the magnetic properties	67
5.6	Magnetoresistance Measurement	71
5.7	Study the temperature dependence of Resistivity of Alnico v (Four probe method)	73
5.8	Impedance and magnetic permeability versus frequency	76
5.9	Compare with impedance and permeability at room temperature ribbon and powder form.	82
	References	85

CHAPTER 6 CONCLUSIONS

5.1	Conclusions	86
5.2	Suggestions for Further Work	87

List of Figures

Fig 2.1:	Permanent Magnets History in the Aspect of Magnet Energy	9
Fig. 2.2:	Phase diagram and free energy curve of spinodal decomposition	11
Fig. 2.3:	Composition profiles of spinodal decomposition and nucleation& growth	11
Fig .2.4:	Magnetic hysteresis loop of three high-energy Alnico grades: Alnico 5 (black), Alnico 8 (red) and Alnico 9 (blue). The higher Br for the Alnico 5 and 9 are consistent with their high grain alignment relative to the applied field direction during processing compared to Alnico 8, which has randomly oriented grains	12
Fig.2. 5:	HAADF STEM images and schematic of α_1 phase morphology of different Alnico alloys: (a) Alnico 5,transverse; (b) Alnico5, longitudinal; (c) model of α_1 phase in Alnico 5; (d) Alnico 8, transverse; (e) Alnico 8, longitudinal; (f) model of α_1 phase in Alnico 8; (g) Alnico 9, transverse; (h) Alnico 9, longitudinal; (i) model of α_1 phase in Alnico 9.	13
Fig. 2.6:	Relation between coercive force and aging time at 600 °C for the Fe-24Co-14Ni-8Al-3Cu alloy after continuous cooling in magnetic field from 900 °C to 600 °C at various cooling rates. Solution treatment was performed at 1250 °C for 1h.	16
Fig.2.7:	Electron micrographs of Alnico 8 specimens annealed for 10 minutes in a magnetic field at (a) 750 °C, (b) 780 °C, (c) 810 °C and (d) 830 °C, respectively. The upper row corresponds to the specimen surface parallel to the applied field and the lower row corresponds to the surface perpendicular to the field	17
Fig. 2.8:	TEM of Alnico 8 thin foils perpendicular to the applied magnetic field. (a) bright-field image of 34 wt% Co Alnico; (b)36 wt% Co Alnico;(c) 40 wt% Co Alnico.	19
Fig. 2.9:	Relation between magnetic properties and Ti content in Alnico 8-type alloys under the optimal isothermal heat treatment.	21
Fig. 2.10:	Electron micrographs of Alnico 8-type alloys containing various Ti content, after the optimal isothermal treatment followed by aging. (a)No.3 (3.10 wt% Ti) (b) No.5 (4.36 wt% Ti) (c) No.7 (6.39 wt% Ti) (d) No.8 (7.52wt% Ti)	21

Fig.2.11:	Effect of added Niobium on the magnetic properties of sintered Alnico 5 magnet alloys	23
Fig. 3.1:	Schematic diagram of arc melter.	26
Fig. 3.2:	Schematic diagram of melt spinner.	27
Fig 3.3:	Melt-spinning apparatus	28
Fig. 3.4:	Schematic representation of a hysteresis loop for a ferromagnetic material portraying the saturation points (a and d), remanence points (b and e), and coercivity points (c and f)	29
Fig. 3.5:	Schematic representation of the magnetic domains with increasing and decreasing magnetizing force	30
Fig.3.6:	Bragg diffraction. Two beams with identical wavelength and phase approach a crystalline solid and are scattered off two different atoms within it. The lower beam traverses an extra length of $2d\sin\theta$. Constructive interference occurs when this length is equal to an integer multiple of the wavelength of the radiation	32
Fig.3.7	Scanning Electron Microscopy	32
Fig3.8:	VSM measurement system	33
Fig 3.9:	magnetoresistance measurement system	33
Fig 3.10:	Wayne kerr impedance analyzer	34
Fig 4.1:	Variation of the chemical and coherent spinodal with composition. The region within which two phases are stable is called the miscibility gap	40
Fig 4.2:	The progression of the sinusoidal composition profile through time	41
Fig 4.3:	A typical evolution sequence for the Cahn-Hilliard equation, where u represents the concentration. As time progresses the concentration approaches a sinusoidal composition profile, as that of spinodal decomposition	43
Fig 4.4:	A numerical solution to the Cahn-Hilliard equation, demonstrating spinodal decomposition. The system begins at an unstable concentration (a), and decomposes into two distinct phases with a characteristic length scale (b, c); as time progresses, the length scale coarsens while maintaining fixed phase concentration fractions.	44
Fig 4.5:	The sequences of formation of a two-phase mixture by nucleation and growth (above) and spinodal decomposition	45

Glossary

α	High temperature B2 single phase
α_1	Fe-Co rich phase spinodally decomposed from α , B2 structure
α_2	Ni-Al rich phase spinodally decomposed from α , L2 ₁ structure
α_γ	Low temperature allotropic transformation of γ phase to bcc structure
γ	Harmful Fe rich grain boundary phase, fcc structure
ϵ	Fe ₂ Ti Laves-type phase, hcp structure
σ	Harmful Co-Ti-Al rich grain boundary phase, possible L2 ₁ structure
ADZ	Aluminum depleted zones Draw Long time (4-48 hrs) low temperature anneal
HIP	Hot isostatic pressing
MA	Magnetic anneal
RE	Rare earth
SPS	Spark plasma sintering

A c k n o w l e d g e m e n t s

The fulfillment of any work requires the support of many people. At the very first, I express my satisfaction to praise the almighty Allah who has given me strength and opportunity to complete my thesis work.

Regarding the outcomes and completion of this thesis work, I express my deepest sense of gratitude and profound respect to my supervisor Prof. Dr. Md.Feroz Alam khan , Department of Physics, BUET, for his invaluable time dedication, close supervision, inspiration and helpful attitude provided during the work as well as for acquainting me with the arena of advanced sresearch.

I am thankful to Dr. Md.Feroz Alam khan Department of Physics, BUET, for their cooperation, affection and inspiration throughout the work.

I am thankful to the authority of BUET for giving me necessary permission and providing with the financial support for this research work.

Finally, I would like to express my gratitude to my beloved wife and all other family members for their multifaceted support through all these years during my work.

Md.Mahamudul Hasan

January , 2017

A b s t r a c t

The structural and thermomagnetic properties of melt-spun Alnico V magnetic ribbons have been studied as function of temperature and magnetic field. Ribbons fabricated at different wheel speeds (25 m/s – 50 m/s) have been studied for their thermal , structural and magnetic properties. The effect of wheel speed on the magnetic properties have been investigated. It is found that change in wheel speed has an effect on the ductility of the ribbons. All the as made and annealed samples have shown pure crystalline structure as revealed by the X-ray Diffraction analysis unlike most of the iron, cobalt and nickel based ribbons which show amorphous or glassy structure after melt-spinning. A significant enhancement in coercive field has been observed after subjecting the Alnico V ribbons through regular heat treatment followed by the aging process. It is observed through this studies that aging the ribbons at high temperature has a positive effect on the coercivity enhancement of Alnico V alloy. The as made ribbons have a relatively low coercivity and only a uniaxial anisotropy is observed which is induced due to mechanical stress developed during meltspinning. However annealing at high temperature followed by aging has yielded a significant increase in coercivity. Elemental addition of Boron has shown to have no effect on the microstructure of the ribbon except for improving the elastic properties of the ribbon. The magneto resistance behavior is found to be typical in nature and has shown a minimum around 1 kOe which is also near the coercive field obtained after Alnico regular heat treatment followed by aging. No significant change is observed in the differential thermal analysis meaning that no structural phase transformation has taken place. However a selective annealing under an external applied magnetic field has caused the nucleation of a crystalline and amorphous mixed phase still dominated by the crystalline phase. It is proposed that this behavior of the alloy at elevated temperature is related to the onset of spinodal decomposition of the alloy where the strong magnetic phase is split into two different magnetic phases with one phase magnetically stronger than the other and the relatively weaker phase grows at the expense of stronger phase causing the deterioration of the overall magnetic properties of the ribbon shaped alloy.

CHAPTER 1

1.1 INTRODUCTION

In recent years there has been a marked shift towards environmental awareness in the areas of energy and transportation. In 2012, the Environmental Protection Agency passed new legislation tightening emissions standards in progressive steps from 2012 to 2025 [1]. Cars and light trucks model year 2025 and after will have a required fuel economy at or greater than 54.5 miles per gallon (mpg). In order for the “2025 Challenge” to be realized, considerable steps will have to be made in alternative energies and vehicle technologies. Alternative fuels such as bio fuels or hydrogen could lower greenhouse gas emissions while still using traditional or modified internal combustion engines. All-electric motors would be nearly emission-free, and therefore even more advantageous. Of the types of electric motors, permanent magnet (PM) based synchronous motors have several advantages; they are typically more compact, lighter in weight, quieter, and require less maintenance [2]. This only holds true if the permanent magnets are sufficiently energy dense, such as neodymium iron boron or samarium cobalt magnets. Rare-earth (RE) magnets and rare-earth materials have increasingly been used in technological devices. High demand for critical RE elements such as dysprosium and neodymium have caused the major source country, China, to enact strict export limits. Limited global supply has caused large price fluctuations, which are undesirable if PM motors are to stay competitive and maintain a reasonable price/performance ratio. A permanent magnet that maintains a high maximum energy product while using abundant, relatively inexpensive elements would be attractive. Alnico

magnets, which are already an industrially produced magnet type, are an Fe-Co based alloy with significant Al, Ni, Cu, and Ti additions. Grades with the highest energy product, alnico 5 is noteworthy due to their high Curie temperature ($\sim 850^\circ\text{C}$), and low temperature dependence of energy product ($\sim 0.2\%/^\circ\text{C}$).

Alnico magnets have not seen any significant advancement in composition or processing since the mid-1970s due to the rise in popularity of the rare-earth based magnet. At the time, research and alloy design were done empirically, making small variations in composition and observing the change in magnetic properties [3]. In the last decade, advances in computational modeling and characterization have made it possible to reexamine alnico. Computations by R. Skomski *et al.* show that in an optimally segregated spinodal system, theoretical energy product of alnico is in excess of current values (5-9 MGOe for later grades), with a maximum of $\mu_0 M_r^2/12$ when the volume fraction of the magnetic phase is $2/3$ total volume [4]. A target maximum energy product of 20 MGOe at 80°C is a performance/price point that would allow alnico to compete with RE permanent magnets, and is achievable according to the theoretical calculations.

1.2 Purpose of Study

Recent studies have shown that alnico forms a nanoscale bcc-intermetallic spinodally decomposed structure [5,6]. The major mechanism of coercivity in alnico is shape anisotropy, which is developed through a complex series of heat treatments that were empirically established [3]. If the heat treatment effects on microstructure of the alnico system could be understood, then alloy processing could be improved to achieve the 20 MGOe target energy product target for PM motors.

Alnico was primarily used for this study due to its already high coercivity (1900 Oe) and equiaxed grain structure. Using this alloy grade, the goal was to investigate current heat treatment processes and their effect on microstructure and magnetic properties, and how the performance of the alloy could be improved using different processing methods. Each step of the conventional heat treatment process was examined for changes to microstructure and magnetic properties. Cast, sintered blended powder, and homogenous gas-atomized powder techniques were also studied for effects on magnetic properties and microstructure development.

1.3 Objectives

Our study aims to optimize the thermal treatment processing and composition of Alnico alloys. Different solidification rate of melt-spun Alnico ribbons created different grain features compared with cast and sintered Alnico. The investigation of the relationship between grain microstructure and magnetic properties are important for coercivity enhancement, since the methods to improve the coercivity of Alnico is deficient. A non-magnetic (γ) phase in Alnico is detrimental to its magnetic properties, therefore, it is necessary to develop methods to get rid of it. Specifically, the objectives of our research are as follows:

- i. Investigation of the structural and magnetic phase transition as a function of magnetic field and temperature.

- ii. Analysis of the structural information and surface morphology of Alnico V magnetic ribbon will be studied.
- iii. Investigation of compositional information of Alnico V magnetic ribbon.
- iv. Study of the temperature dependent electrical resistivity.
- v. Investigation of the magneto resistance, and magnetic permeability.
- vi. To study the effect of heat treatment and composition on magnetic properties of melt-spun Alnico alloys;
- vii. To investigate the effect of solidification process on the grain micro structural and magnetic properties of melt-spun and cast Alnico alloys;

1.4 Outline of this thesis

The summary of the thesis is as follows:

Chapter 1 represent the the General Introduction of this thesis.

Chapter 2 gives a brief overview of the materials, theoretical background as well as crystal structure of the alnico v magnet.

Chapter 3 gives the details of sample preparation and description of different measurement techniques that have been use in this research work.

Chapter 4 gives the idea of mathematical and theoretical background of spinodal decomposition.

Chapter 5 is devoted to the result of various investigations of the study and explanation results in light of existing theories.

Chapter 6 Includes the conclusions and suggestion for future work.

References:

- [1] Murphy, J., “Permanent-magnet AC motors”, Machine Design, 2012.
- [2] R. A. McCurrie, “The Structure and Properties of Alnico Permanent Magnet”, Alloy, Ferromagnetic Mater., vol. 3, E. P. Wohlfarth, Ed. Bradford: North-Holland Publishing Company, pp. 107–188, 1982
- [3] R. Skomski, Y. Liu, J. E. Shield, J. E., Hadjipanayis, G. C., and D. J. Sellmyer, “Permanent magnetism of dense-packed nanostructures”, J. Appl. Phys., vol. 107, pp. 567–572, 2010.
- [4] J. M. Aquino, C. D. Rios, M. M. Yoshida, M. M., and Valenzuela, O. A., “Magnetic properties and microstructure of the alnico 8”, Mater. Sci. Forum, vol. 302–303, pp. 329–333, 1999.
- [5] C. H. Liebscher, V. Radmilovic, U. Dahmen, U., Asta, M., and Ghosh, G., “On the formation of hierarchically structured L_{21} -Ni₂TiAl type precipitates in a ferritic alloy”, J. Mater. Sci., vol. 48, pp. 2067–2075, 2013.
- [6] D. Jiles, “Introduction to Magnetism and Magnetic Materials”, 2nd ed. Boca Raton, FL: Taylor & Francis Group, 1998.
- [7] First4Magnets, “Hysteresis Graph Example”, Strongest Magnets, 2013.

Chapter 2 Literature Review

2.1 History of Alnico Alloys

Alnico permanent magnets were developed in early 1930s by Japanese scientist Tokushichi Mishima[1,2]. He developed permanent magnet made from nickel, aluminum and iron with better magnetic properties than "magnet steels" available at the time. A few months later, he reported addition of cobalt (Co) could further enhance the magnetic properties of the alloy [3].

In 1935, researcher William E. Ruder of General Electric developed a new Alnico permanent magnet. An Alnico disk of less than a pound can be used to swing a 55-lb. radio cabinet. This suggested that Alnico was ready to replace small electromagnets in motors, transformers, and loudspeakers, which show great potentials in lowering the cost and simplifying the construction[4]. Anisotropic Alnico alloys with columnar grains were developed by Gottfried Bruno Jonas of the Netherlands in late 1930s. Such alloys show 50% to 200% higher maximum energy product than isotropic Alnico[4]. Since that time, Alnico had been developed into a robust permanent magnet. However, commercial exploitation of this material was stopped by the advent of World War II. It was not until 1947 that Alnico speakers was used in guitar amps of Gibson and Fender[4], which indicated the rise of Alnico products. Figure 1 shows an advertisement from QST amateur radio magazine released in April 1945, exhibiting importance of Alnico. Since researchers cannot further improve the remanence of Alnico, they switched their attention to coercivity enhancement. Koch *et al.* found Ti-containing Alnico has better coercivity, followed by the development of Alnico 8[5]. However, Ti introduces grain

refinement, which makes it difficult to obtain a columnar structure. At that time there was considerable doubt in the Alnico industry that any practical results could be achieved[6].

In the early of 1960s, Gould discovered that appropriate sulfur (S) addition to Alnico 8 produced columnar crystals without sacrificing large magnetic properties[7,8]. Since then, further work on composition modification to improve coercivity without reducing remanence led to the introduction of Alnico 9 in the U.S. market in 1964[6]. Research on Alnico stopped after 1975, after the emergence of high coercivity rare earth permanent magnets, such as samarium cobalt and neodymium iron boron. There has been no significant progress on magnetic properties of Alnico since 1964, as can be seen in Figure 2.1 Today, researchers are focusing on understanding coercivity

Mechanisms[9,10], microstructure[11], and processing[11,12] to improve its magnetic properties.

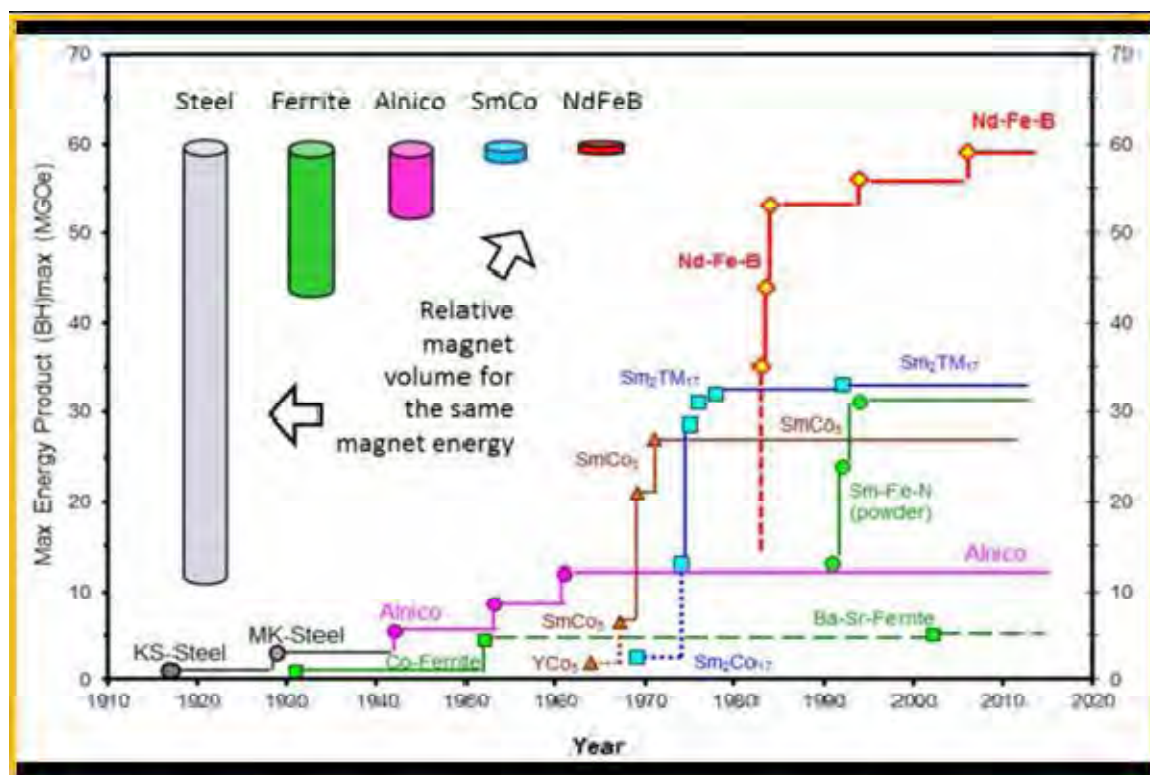


Figure 2.1. Permanent Magnets History in the Aspect of Magnet Energy[10]

2.2 Magnetic origin of Alnico Alloys

Magnetic properties of Alnico are resulted from the phase transformation (spinodal decomposition). A α_1 (Fe-Co rich) and α_2 (Al-Ni rich) phases are developed in Alnico after spinodal decomposition, in which α_1 phase is strong ferromagnetic, while α_2 is weakly ferromagnetic. α_1 phase is aligned as rods in $\langle 100 \rangle$ direction and distributed in α_2 phase, since $\langle 100 \rangle$ is the energetically favorable direction[14].

Spinodal decomposition is a continuous phase transformation arising from conserved order parameter, which means it cannot change in one location without affecting its neighborhood [15]. As can be seen in Figure 3, an alloy with composition X_0 is heat treated at T_1 and then quenched to T_2 . Its composition is homogeneous and initial free energy is G_0 at the beginning. However, the alloy will be immediately unstable due to small variations in composition, producing A-rich and B-rich phase will reduce the total free energy. Therefore, „up-hill“ diffusion occurs until the equilibrium composition X_1 and X_2 are achieved [16]. There is no activation energy barrier inside the spinodal area. If the alloy lies outside the spinodal area, small fluctuation of composition results in free energy increase, and the alloy is metastable. In order to reduce the free energy of the system, nucleation and growth will take place. Therefore, „down-hill“ diffusion occurs in this situation, as can be seen in Figure 4. There are three high-energy Alnico alloys, which are Alnico 5, Alnico 8, and Alnico 9. Figure 5 shows magnetic properties of these three Alnico grades. Alnico 5 has the highest remanence compared to other two grades. However, Alnico 8 has the maximum coercivity. Alnico 9 combines characteristics of Alnico 5 and Alnico 8, showing the maximum energy product. The difference of magnetic properties among these Alnico alloys results from various chemical composition, followed by shape anisotropy variation

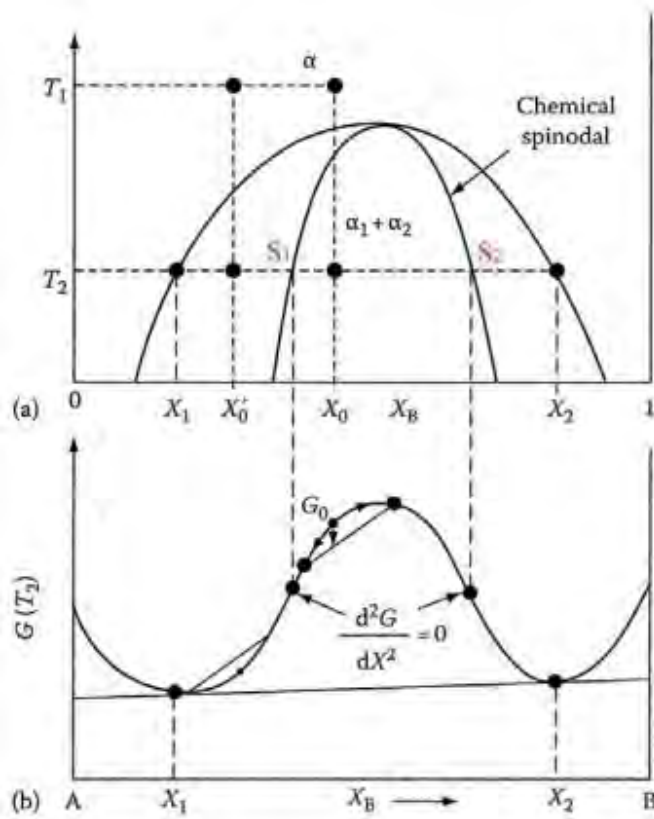


Figure 2.2. Phase diagram and free energy curve of spinodal decomposition[16].

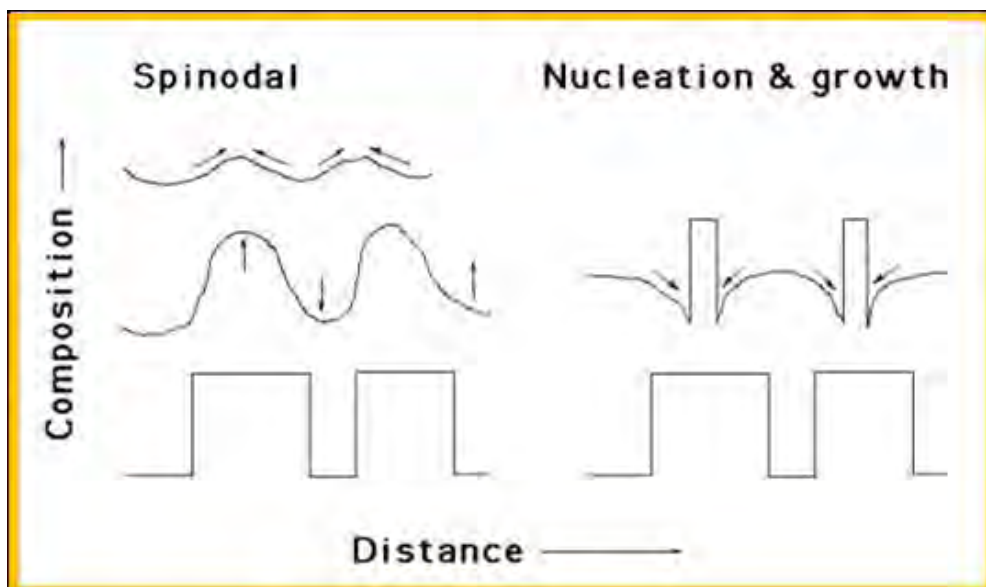


Figure 2.3. Composition profiles of spinodal decomposition and nucleation & growth[16].

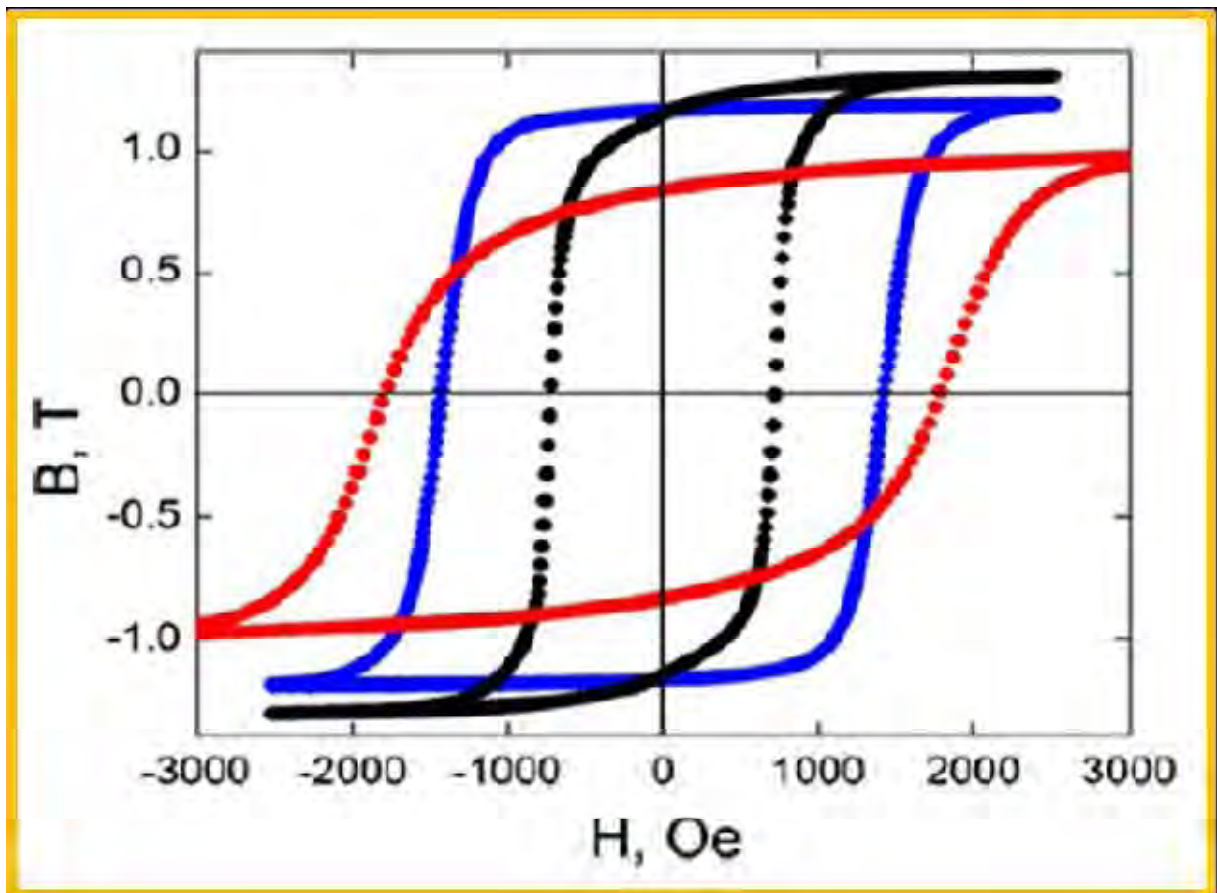


Figure 2.4. Magnetic hysteresis loop of three high-energy Alnico grades: Alnico 5, Alnico 8 and Alnico 9 . The higher B_r for the Alnico 5 and 9 are consistent with their high grain alignment relative to the applied field direction during processing compared to Alnico 8, which has randomly oriented grains[9].

The coercivity of Alnico is largely determined by shape anisotropy[10,17]. Figure 5 shows high-angle-annular-dark-field (HAADF) scanning transmission electron (STEM) imaging, which clearly differentiates phase morphology in Alnico alloys[10]. The aspect ratio of α_1 phase in Alnico 5 is about 5, however, Alnico 8 and Alnico 9 has larger aspect ratio, which are around 10.

$$H_{ci} = (1 - \rho)(N_b - N_a)C^{\text{Fe+Co}} M_s^{\text{Fe,Co}}$$

where ρ is volume fraction of α_1 phase, N_b is demagnetizing factor along the long axis, N_a is demagnetizing factor along the short axis, C^{Fe+Co} is the relative concentration of $Fe+Co$ in the α_1 phase, $M_s^{Fe,Co}$ is saturation magnetization of the sample.

Equation [10] shows that the intrinsic coercivity of Alnico alloys is proportional to the difference in the demagnetizing factor between the long axis and the short axis. Therefore, a high aspect ratio of α_1 phase is beneficial for coercivity improvement. This characteristic is used to design high coercivity Alnico alloys.

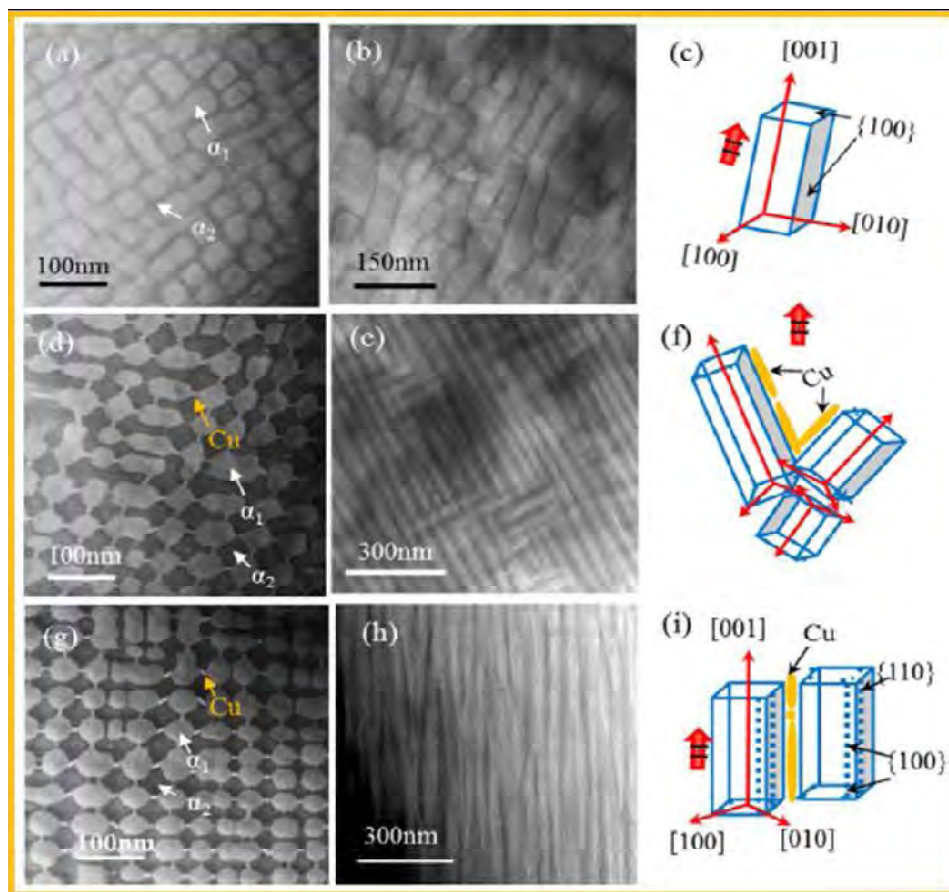


Figure 2.5. HAADF STEM images and schematic of α_1 phase morphology of different Alnico alloys: (a) Alnico 5, transverse; (b) Alnico 5, longitudinal; (c) model of α_1 phase in Alnico 5; (d) Alnico 8, transverse; (e) Alnico 8, longitudinal; (f) model of α_1 phase in Alnico 8; (g) Alnico 9, transverse; (h) Alnico 9, longitudinal; (i) model of α_1 phase in Alnico 9 [10].

2.3 Manufacturing Process

Commercial Alnico alloys are fabricated by casting and sintering. For cast Alnico, pure elements are put into a furnace and melted at 1750-1780 °C. The molten Alnico alloy is poured into sand molds with required shape of magnet. The sand mold and casting is cooled rapidly to avoid the formation of gamma phase. Sometimes there are chilled plates at the bottom of the molds to aid cooling. Sand can be exothermic sand, which gives a different cooling rate. Exothermic sand is combined with chilled plates to

produce textured Alnico alloys with higher remanence values. After cooling, the sand mold is broken down and the magnets retrieved. A series of heat treatments are applied to as-casted Alnico. If required, the magnets are ground to finished size and are also magnetized before packing[13]. Sintered Alnico is made by compacting powder. Firstly, the raw elements are ground

by milling into particles. Secondly, the powder is pressed in a die under tones of pressure. The resulting magnet is then sintered at 1260 °C in a hydrogen atmosphere to melt the powder together. Generally, sintered Alnico magnets are small, weighing less than 30 grams[3].

2.4 Heat Treatment

As-made Alnico alloys are magnetically soft, with the coercivity of a few oersted. Their relatively good magnetic properties are given by heat treatment. Therefore, heat treatment study is very important for improving Alnico alloys' performance. Heat treatment of Alnico alloys

depends on their types. Typically, the heat treatment of Alnico includes three steps. For Alnico 5, samples are heat treated at 1350 °C to reach the single phase, and then are fast cooled to 900 °C. This process is called solutionization, which is used to make homogeneous α phase and remove γ phase formed in Alnico preparation process. Samples are then cooled to 600 °C under a magnetic field where spinodal decomposition takes place. Following a double tempering for 6 hours at 650 °C and 24 hours at 550 °C to achieve chemical equilibrium between α_1 and α_2 phases[18]. For Alnico 8 and Alnico 9, firstly, as made Alnico alloys are solutionalized above 1250 °C for half an hour, and then are quenched to room temperature to achieve single phase.

Secondly, the quenched samples are annealed for 10 minutes at 800 °C in the presence of a magnetic field for spinodal decomposition development[19]. The magnetic properties of Alnico alloys are mainly determined in this process. Field annealing samples are successively annealed at 650 °C and 550 °C as Alnico5, to sharpen phase separation, followed by magnetic properties improvement. Kim *et al.* reported the effect of cooling rate and low temperature solutionization on the magnetic properties of Alnico 5[20]. They found the magnetic properties of Alnico 5 are highly dependent on the cooling rate from 900 °C to 600 °C. The faster the cooling rate is, the smaller the size and the larger aspect ratio of α_1 phase it will have, resulting in better coercivity, as shown in Figure 2. 7.

Iwama *et al.* studied the effect of isothermal annealing temperature on evolution of phases, as can be seen in Figure 2. 11. The quenched specimens were isothermally annealed at 750, 780, 810, and 830 °C, respectively, with a magnetic field applied along the columnar axis of the specimen. It shows α_1 phases aligned along the magnetic field direction, and 810 °C producing the optimal morphology[14].

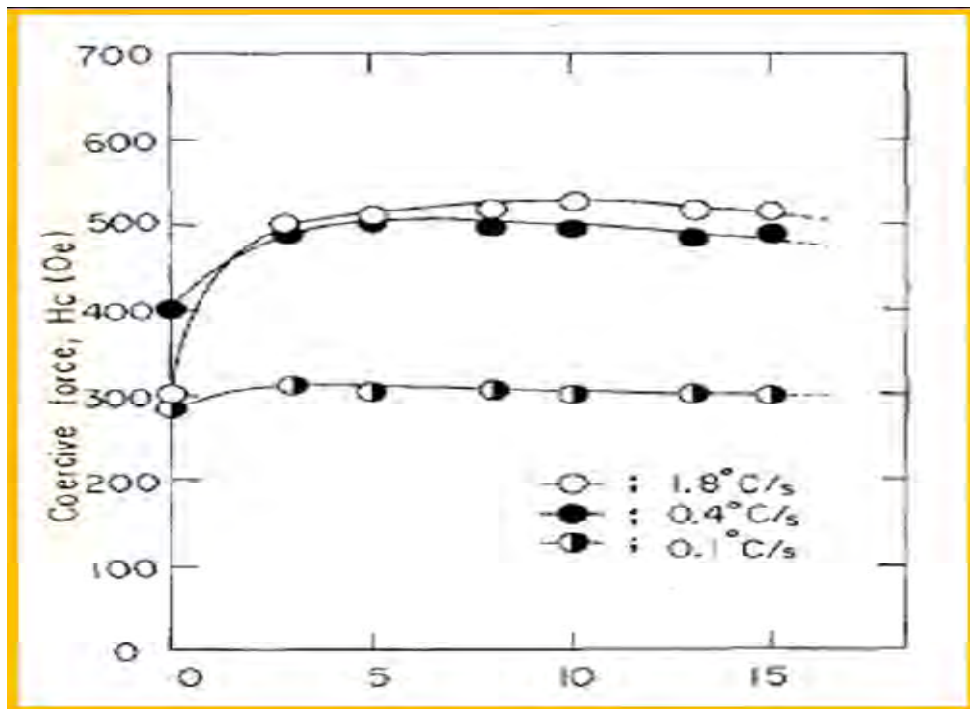


Figure 2.6. Relation between coercive force and aging time at 600 °C for the Fe-24Co-14Ni-8Al-3Cu alloy after continuous cooling in magnetic field from 900 °C to 600 °C at various cooling rates. Solution treatment was performed at 1250 °C for 1h[20].

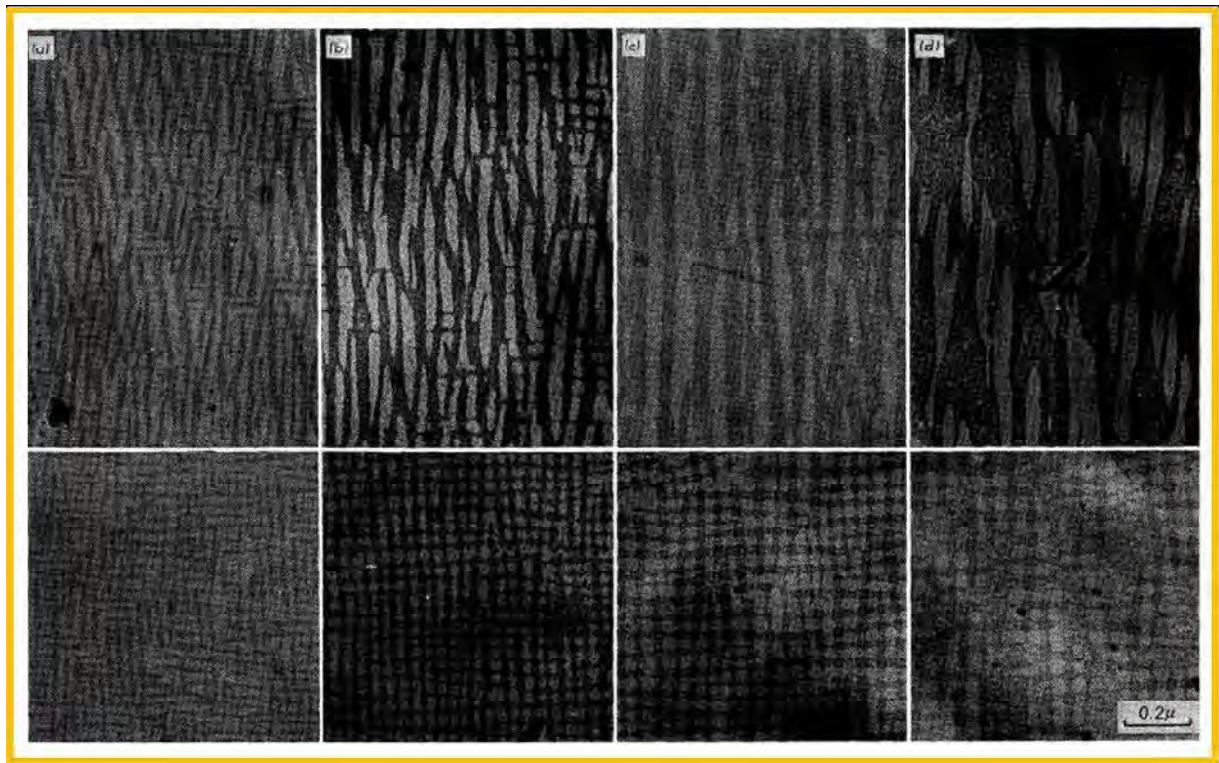


Figure 2.7. Electron micrographs of Alnico 8 specimens annealed for 10 minutes in amagnetic field at (a) 750 °C, (b) 780 °C, (c) 810 °C and (d) 830 °C, respectively. The upper row corresponds to the specimen surface parallel to the applied field and the lower row corresponds to the surface perpendicular to the field[14].

2.5 Alloy Addition

Alloy additions are an effective way to improve magnetic properties of Alnico alloys by controlling shape anisotropy and microstructures. The alloying elements for Alnico can be separated into two categories: (1) Elements that are used to boost intrinsic coercivity of Alnico, and (2) elements to help columnar grain growth. The main challenge of Alnico V is its deterioration of the magnetic properties at elevated temperature, e.g., above 1100C. Suitable replacement of elemental composition is a way to sustain and even enhance the magnetic properties of this alloy at high temperature. Fabrication process of this alloy is also important .

Alnico V is a permanent magnet and retains its crystallinity in any form . Fabricating Alnico V by hard pressing the powder (solid state technique) has been proven useful . Melt-spinning the alloy is rather new technique and there are not many information available on the magneto-transport properties of melt-spun Alnico V. In this work in addition to melt spinning the Alnico V ingot the addition of B and also its effect on the elastic and magneto-transport properties have been investigated.

2.6 Coercivity Enhancers

Most of Co goes to α_1 phase after spinodal decomposition, which increases saturation magnetization, resulting in higher Br . Equation 2 shows this also enlarges the magnetization difference between α_1 and 2. H_c results from magnetostatic interactions, as can be seen in equation 3 [46]. Therefore, the coercivity of Alnico is increased with Co addition. Here ΔM is the difference in saturation magnetization, M_{α_1} the saturation magnetization of α_1 phase, M_{α_2} the saturation magnetization of α_2 phase, N_2 the demagnetizing factor along the long axis, and N_1 demagnetizing factor along the short axis.

$$\Delta M = M_{\alpha_1} - M_{\alpha_2} \quad (2)$$

$$H_c \propto \Delta M (N_2 - N_1) \quad (3)$$

. Liu *et al.* investigated Alnico alloys containing 34, 36, 38, and 40 wt% Co[27]. They found that there was more α_1 phases with diameter smaller than 10nm when increasing Co and Ti content in the samples, as can be seen in Figure 13. The coercivity largely increases with Co, while the remanence and squareness of the demagnetization curve decrease with Co. They explained that the increasing nonmagnetic Ti content is the reason for saturation magnetization reduction.

However, there is no report of Ti content of their specimens. It is possible that particle alignment and perfection deteriorate with Co, following with the reduction in saturation magnetization.

Table 1. Magnetic properties of Alnico 8[27].

Alnico 8 (mass%) Co	B_r (T)	H_{cj} (kA/m)	$(BH)_{max}$ (kJ/m ³)	H_k/H_{cj}
34Co	1.14	117	93.5	0.89
36Co	1.13	126	104.3	0.88
38Co	1.08	132	97.9	0.85
40Co	1.04	144	93.4	0.83

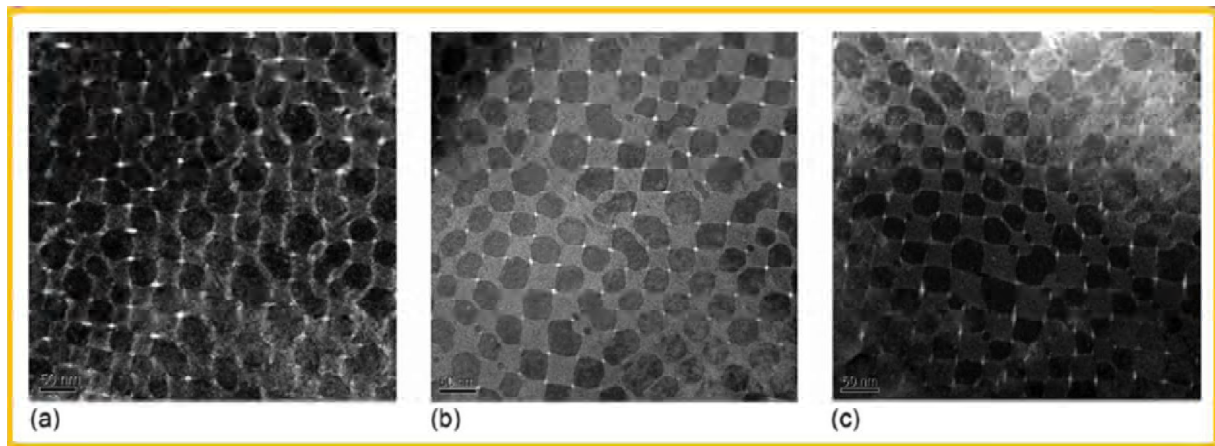


Figure 2.8. TEM of Alnico 8 thin foils perpendicular to the applied magnetic field. (a) bright-field image of 34 wt% Co Alnico; (b) 36 wt% Co Alnico; (c) 40 wt% Co Alnico[27].

Ti is another element that can boost coercivity of Alnico alloys. Alnico 8 and Alnico 9 are well-known due to their relatively high coercivity compared with Alnico 5, especially when an isothermal field treatment is applied[48]. Coercivity enhancement can be explained by the

equation 2 and 3. Ti is a paramagnetic element, which primarily segregates to the α_2 phase [30]. This can increase the saturation magnetization difference between α_1 and α_2 phases, enhancing coercivity. Another reason is that Ti improves the shape anisotropy of Alnico alloys. This is proved by comparison of the aspect ratio of Alnico 5, Alnico 8 and Alnico 9 [30]. Alnico 5 usually has an aspect ratio of 5, while Alnico 8 and Alnico 9 have aspect ratios of 10. Takeuchi *et al.* performed anisotropy measurements using a combination of magnetic measurements and electron microscopy on monocrystalline Alnico alloys [29]. They found that the shape anisotropy constant increases with Ti content, resulting in coercivity improvement. They also found that the packing fraction of the α_1 phase dramatically changes with Ti, leading to the conclusion that one main reason for high coercivity of the high Ti-containing Alnico is the packing fraction. However, this finding does not agree with other work [10], which shows packing fraction has no obvious change among Alnico 5, Alnico 8, and Alnico 9.

Iwama *et al.* studied the effect of Ti in Alnico 8-type alloys [28]. Figure 14 shows that extrinsic coercivity (BH_c) significantly increases as Ti content increases. It approaches 1700 Oe at 6 wt% Ti, and then slightly decreases. At the same time, B_r linearly decreases with Ti. The optimal Ti content is 5 wt%, which shows the highest (BH)_{max}. The electron microscopy images in Figure 15 reveal the precipitates particles after optimal heat treatment are likely to coarsen in both size and aspect ratio with increasing Ti. This finding seems to contradict the recent characterization study of Alnico 5, Alnico 8, and Alnico 9 [10], and the later report about the effect of Ti on shape anisotropy [29]. It is likely that shape anisotropy is mainly determined by the synergy of Co and Ti, rather than by Ti itself, since Ti was increased while Co was decreased. On the contrary, high Ti containing Alnico alloys usually have high Co content, which leads to improvement in shape anisotropy and magnetic properties [10,29].

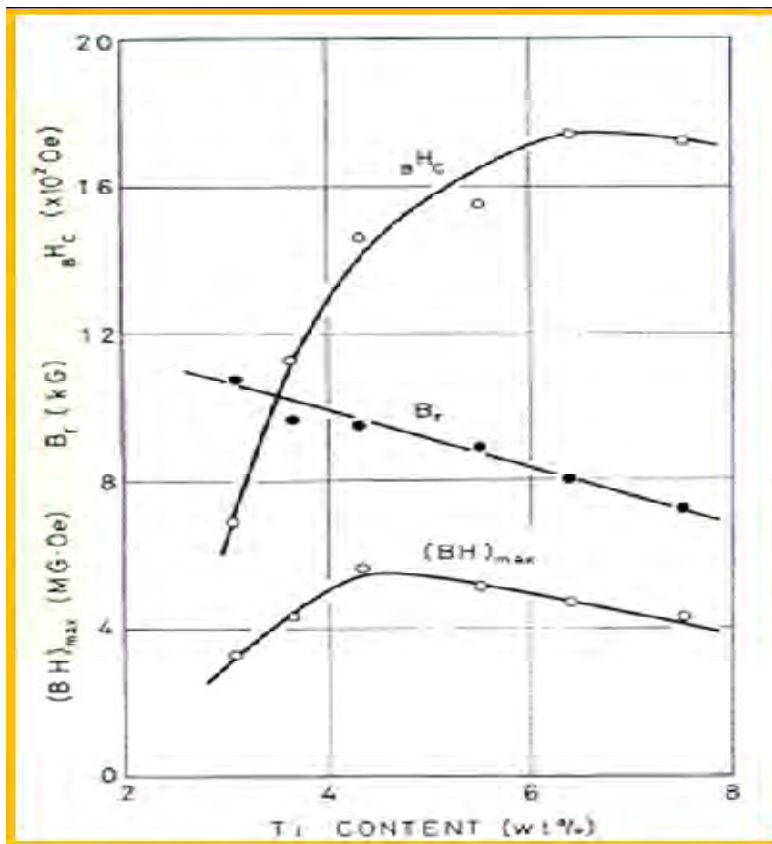


Figure 2.9. Relation between magnetic properties and Ti content in Alnico 8-type alloys under the optimal isothermal heat treatment[28].

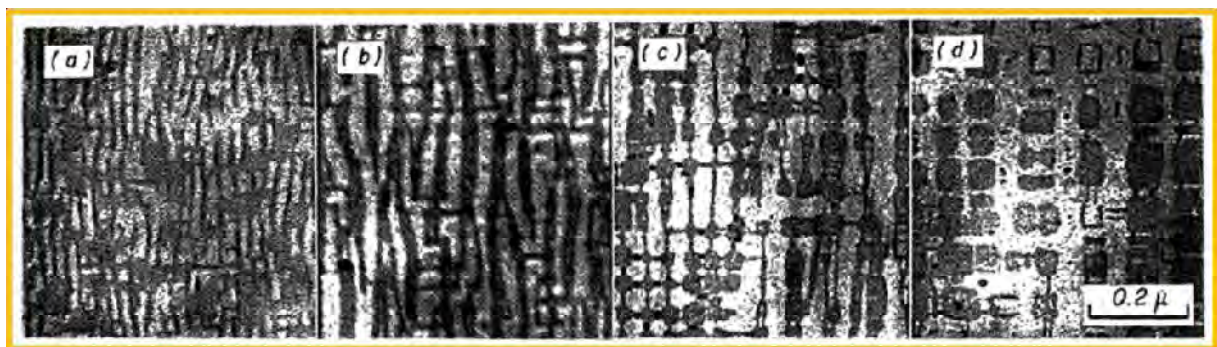


Figure 2.10. Electron micrographs of Alnico 8-type alloys containing various Ti content, after the optimal isothermal treatment followed by aging[28]. (a) No. 3 (3.10 wt% Ti) (b) No. 5 (4.36 wt% Ti) (c) No. 7 (6.39 wt% Ti) (d) No. 8 (7.52 wt% Ti)

Nb is another element that can be used to enhance coercivity. The reason for coercivity enhancement results from shape anisotropy improvement[30]. Although the effect of Nb on the

microstructure of Alnico alloys has not been studied, it is suggested that it is similar to Ti addition[50]. Szymura *et al.* investigated the influence of Nb addition on the magnetic properties of textured Alnico 5 alloy. They found 0.5 wt% Nb addition decrease remanent induction while increasing coercivity and squareness of the hysteresis loop[30]. Sugiyama *et al.* studied the effect of Nb on the magnetic properties of sintered Alnico 5 alloys[51]. As can be seen in Figure 2.10, coercivity increases as Nb increases. However, remanence gradually decreases when Nb addition is over 1%. They also reported large amount of Nb addition cause pore aggregation, rapid grain growth, and negative effects on rupture strength. They suggested that 0.35~0.70 wt% of Nb addition is optimal to improve sintered Alnico 5 alloys.

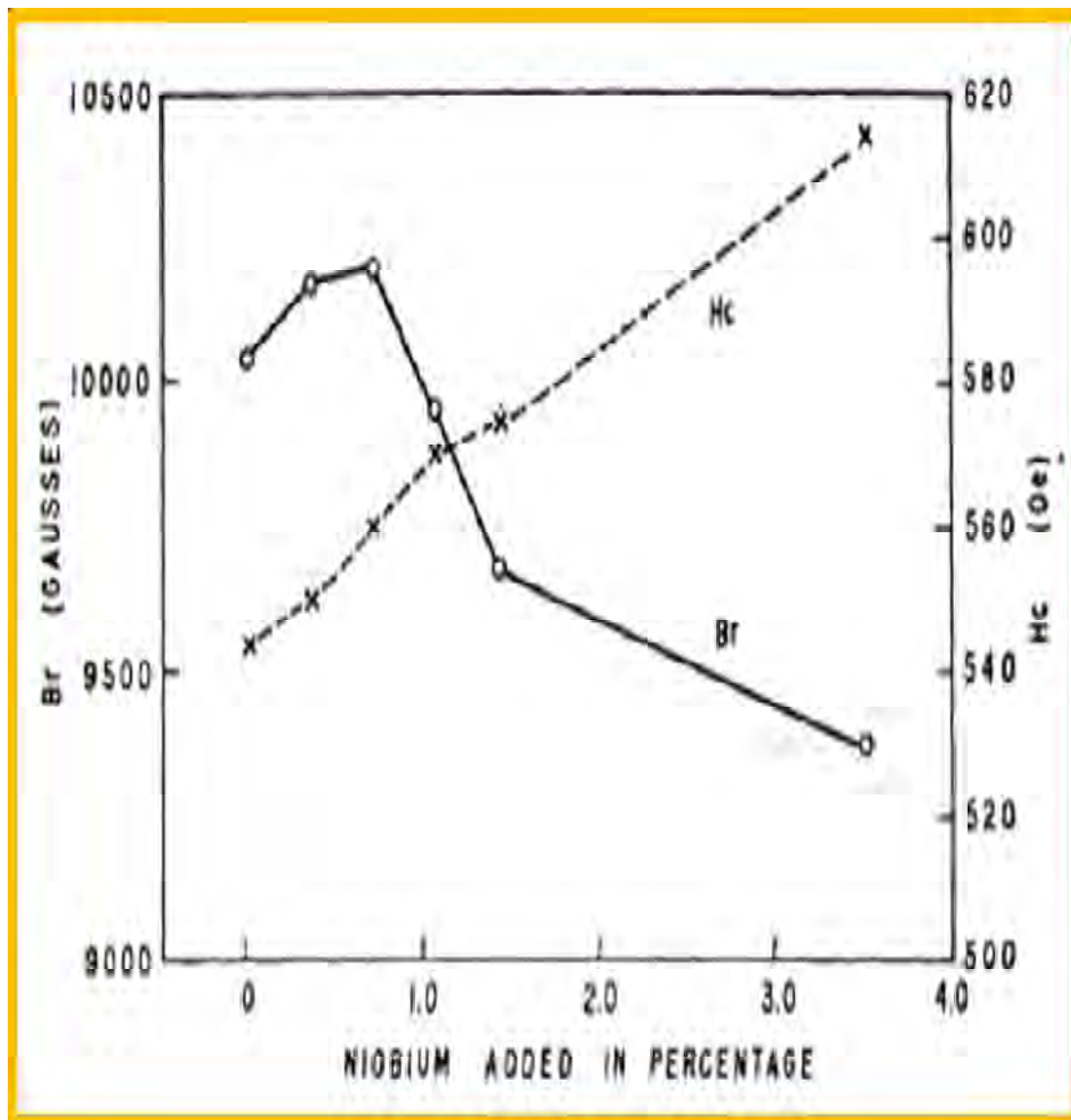


Figure 2.11. Effect of added Niobium on the magnetic properties of sintered Alnico 5 magnet alloys[31].

References:

- [1] A. S. Rao and D. Ph, "Alnico Permanent Magnets," vol. 62, no. 1949, pp. 373–383, 1959.
- [2] E. R. Cronk, "Recent Developments in High-Energy Alnico Alloys," *J. Appl. Phys.*, vol. 37, no. 3, p. 1097, 1966.
- [3] J. E. Gould, "Magnets with columnar crystallization," *Cobalt & Cobalt Abstr*, vol. 23, pp. 82–87, 1964.
- [4] M. McCaig, "Recent developments in permanent magnetism," *J. Appl. Phys.*, vol. 35, no. 3, pp. 958–965, 1964.
- [5] A. Palasyuk, E. Blomberg, R. Prozorov, L. Yue, M. J. Kramer, R. W. McCallum, I. E. Anderson, and S. Constantinides, "Advances in characterization of non-rare-earth permanent magnets: Exploring commercial alnico grades 5-7 and 9," *Jom*, vol. 65, no. 7, pp. 862–869, 2013.
- [6] L. Zhou, M. K. Miller, P. Lu, L. Ke, R. Skomski, H. Dillon, Q. Xing, A. Palasyuk,
- [7] M. R. McCartney, D. J. Smith, S. Constantinides, R. W. McCallum, I. E. Anderson,
- [8] V. Antropov, and M. J. Kramer, "Architecture and magnetism of alnico," *Acta Mater.*, vol. 74, pp. 224–233, 2014.
- [9] W. Tang, L. Zhou, A. G. Kassen, A. Palasyuk, E. M. White, K. W. Dennis, M. J. Kramer, R. W. McCallum, and I. E. Anderson, "New alnico magnets fabricated from pre-alloyed gas-atomized powder through diverse consolidation techniques," *Magn. IEEE Trans.*, vol. 51, no. 11, pp. 1–3, 2015.
- [10] First4Magnets, "Hysteresis Graph Example," Strongest Magnets, 2013.
- [11] T. Mishima, *Ohm*, vol. 19, p. 353, 1932.
- [12] W. Betteridge, "Nickel-Iron-Aluminum Permanent Magnet Alloys," The Iron and Steel Institute. Richard Clay and Company, Ltd., 1939.
- [13] D. A. Oliver and J. W. Shedden, "Cooling of permanent magnet alloys in a constant magnetic field," *Nature*, vol. 142, no. 3587, p. 209, 1939.
- [14] W. Sucksmith, "A magnetic study of the iron-nickel-aluminum system," *Proc. R. Soc. London, Ser. A, Math. Phys. Sci.*, vol. 171, no. 947, pp. 525–540, 1939.

- [15] J. L. Snoek, "Magnetic studies in the ternary system FeNiAl," *Physica*, vol. 6, no. 4, pp. 321–331, 1939.
- [16] R. D. Heidenreich and E. A. Nesbitt, "Physical Structure and Magnetic Anisotropy of Alnico 5. Part I," *J. Appl. Phys.*, vol. 23, no. 3, pp. 352–365, 1952.
- [17] W. Wright and A. Thomas, "Influence of aluminum and titanium on grain structure in alnico-type permanent magnet alloys," *Cobalt*, vol. 13, 1961.
- [18] K. J. De Vos, "Alnico Permanent Magnet Alloys," in *Permanent magnets and magnetism: theory, materials, design, manufacture and applications*, New York: John Wiley & Sons, 1962, pp. 475–512.
- [19] J. W. Cahn and J. E. Hilliard, "Free Energy of a Nonuniform System. I. Interfacial Free Energy," *J. Chem. Phys.*, vol. 28, no. 2, p. 258, 1958.
- [20] J. W. Cahn, "Magnetic aging of spinodal alloys," *J. Appl. Phys.*, vol. 34, no. 12, pp. 3581–3586, 1963.
- [21] J. J. De Jong, J. M. G. Smeets, and H. B. Haanstra, "Some Results of an Electron Microscopical Study of the Metallographic Structure of Two Alloys for Permanent Magnets (Ticonal G and Ticonal X)," *J. Appl. Phys.*, vol. 29, no. 3, p. 297, 1958.
- [22] K. Bradsher, "China consolidates grip on rare earths," *The New York Times*, The New York Times Company, New York, 2011.
- [23] T. Folger, "The Secret Ingredients of Everything," *Natl. Geogr. Mag.*, no. June, 2011. Magnetic Materials Producers Association, "Standard Specifications for Permanent Magnet Materials," *Alnico Magnets*. p. 7, 2000.
- [24] L. Eleno, K. Frisk, and A. Schneider, "Assessment of the Fe-Ni-Al system," *Intermetallics*, vol. 14, pp. 1276–1290, 2005.
- [25] M. Stanek, L. Wierzbicki, and M. Leonowicz, "Investigations of Thermo-Magnetic Treatment of Alnico 8 Alloy," *Arch. Metall. Mater.*, vol. 55, no. 2, pp. 571–577, 2010.
- [26] G. Begin and A. Dube, "On the magnetizations of the phases in alnico alloys," *IEEE Transactions Magn.*, vol. 8, no. 1, pp. 42–45, 1972.

Chapter 3 Experimental Procedure

3.1 Arc Melting

Arc melting or vacuum arc melting is a traditional method used to prepare solid metal ingots. In our process, pure metals were placed on a water cooled copper plate. The chamber of the arc melter was repeatedly pumped and backfilled with high purity argon gas. The base pressure was around 100 m Torr and the operating temperature was slightly below atmospheric pressure. A large voltage was applied to tungsten electrode to generate the arc. Pure metals were melted by the arc with melting temperature up to 3500 °C and then formed a solid sample. The sample was then flipped and re-melted for four times to ensure chemical homogeneity.

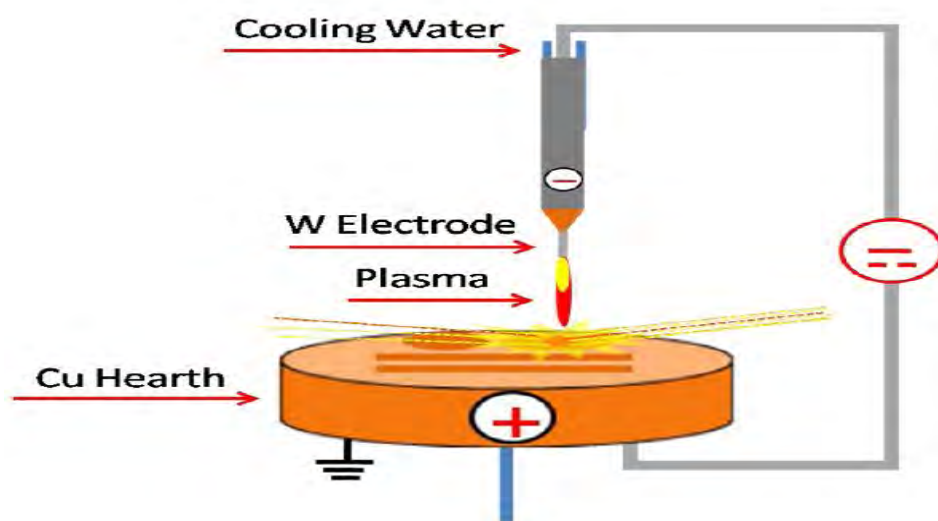


Figure 3.1. Schematic diagram of arc melter.

3.2 Melt Spinning

Melt spinning is a method that can control solidification and structure of materials [38]. In our experiment, the base pressure was 2.3×10^{-2} Torr. Samples were melted by radio frequency induction heat copper coil, and then ejected by over pressured argon through a small round nozzle (0.72 mm in diameter) onto the rotating copper wheel. Alnico ribbons were collected for characterization.

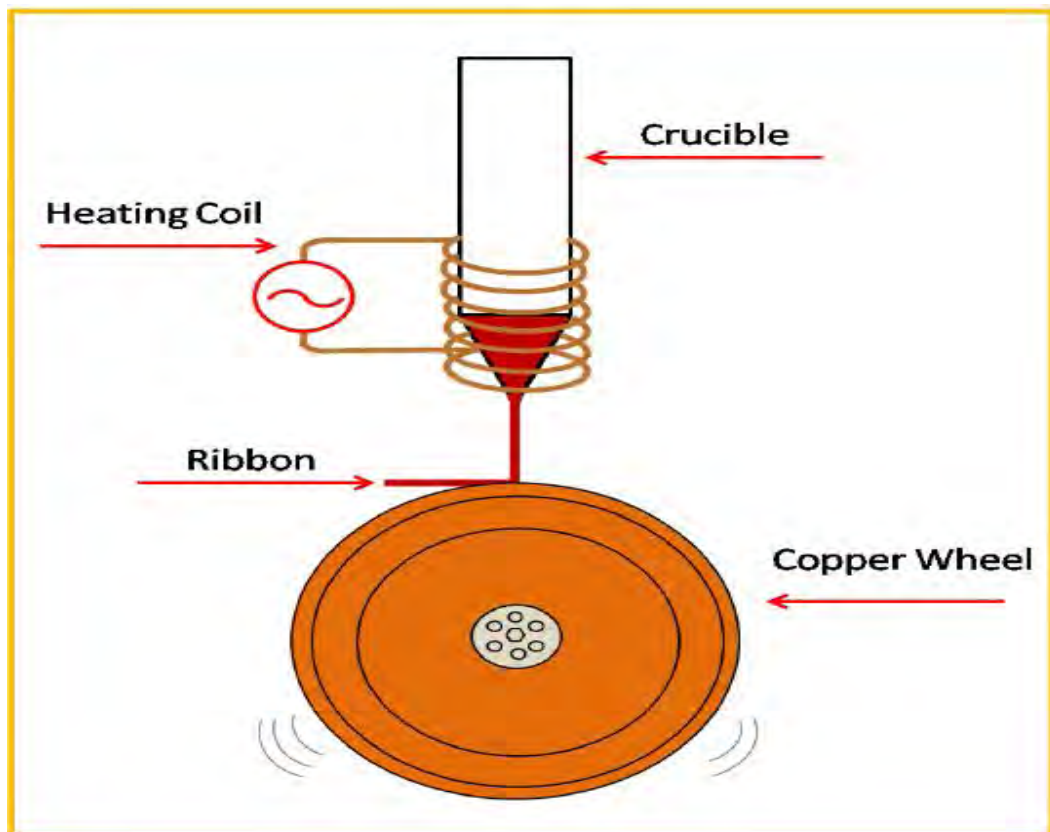


Figure 3.2. Schematic diagram of melt spinner.

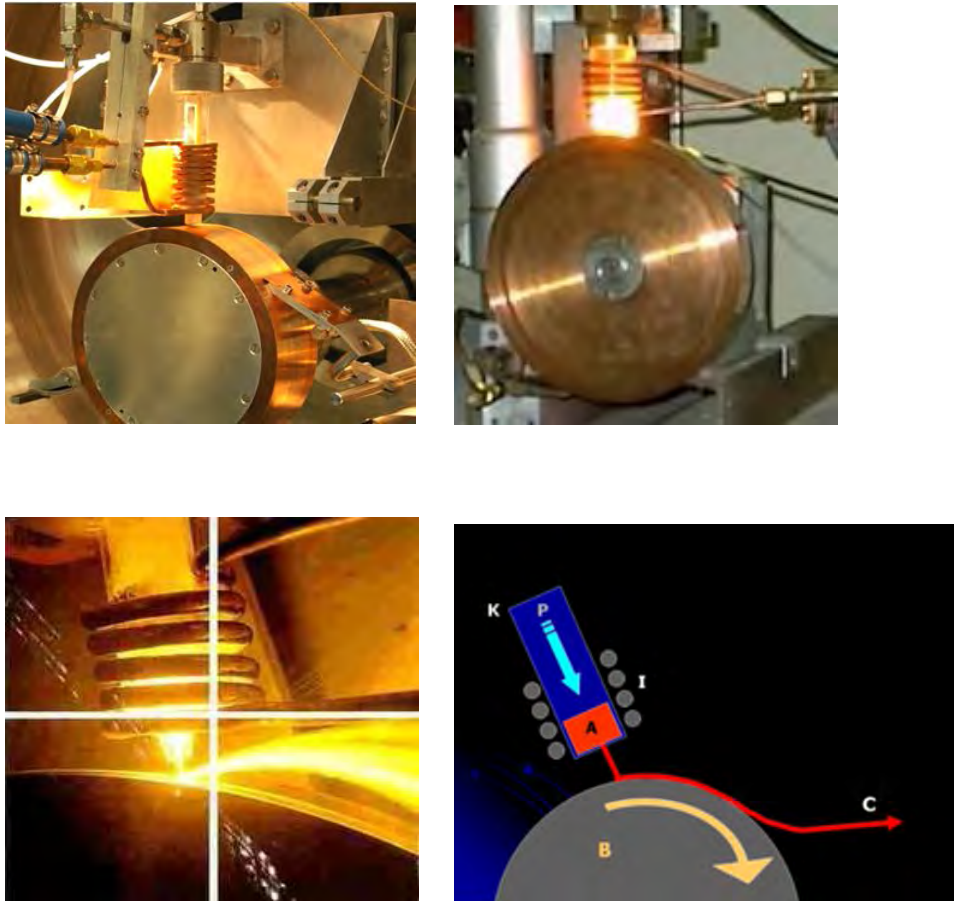


Fig 3.3.Melt-spinning apparatus

3.3 Hysteresis Loop

The hysteresis loop is the fingerprint of a ferromagnetic material, the typical shape can be seen in Figure 3.4, which results from a nonlinear response of ferromagnetic materials to an applied external magnetic field. Any ferromagnetic material is composed of small regions where all magnetic dipole moments align in the same direction, and contiguous domains are separated by domain walls[59]. The hysteresis loop begins at starting point with zero applied field ($H=0$), at this state, all the domains are disoriented such that vector sum of the magnetizations is zero.

When an external magnetic field is applied, the magnetization increase gradually and then rapidly, finally saturate at point a, which is called saturation magnetization. In this point, the specimen becomes a single domain that is aligned in the direction of applied field. When H is reversed and reduced to zero, some magnetization remains, which is known as the remanence (B_r). This may be explained by the resistance to movement of domain walls, corresponding to the increase of H in the opposite direction[39]. In order to remove the remanence, a reversed H is required. The field applied to reduce remanence to zero is called coercivity (H_c). Since all the domains have different magnetization direction, there is no magnetic flux ($B=0$) at point c. With increasing of field in the opposite direction, the same saturation happens as it did before. The cycle is then reversed to get a full hysteresis loop.

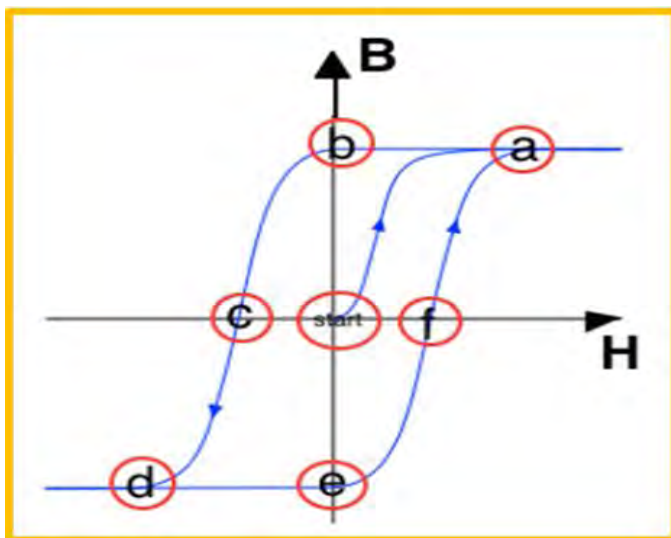


Figure 3.4. Schematic representation of a hysteresis loop for a ferromagnetic material portraying the saturation points (a and d), remanence points (b and e), and coercivity points (c and f)[40].

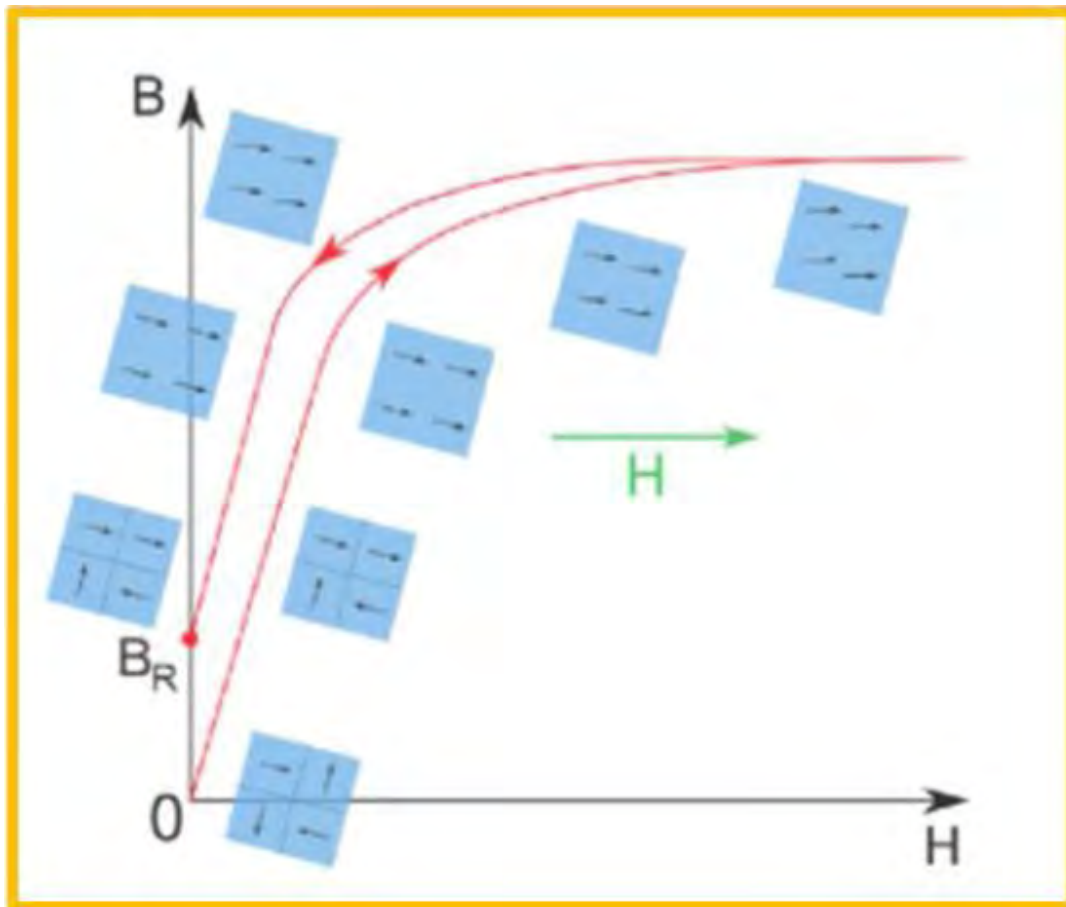


Figure 3.5. Schematic representation of the magnetic domains with increasing and decreasing magnetizing force[40].

Figure 3.5 shows magnetic domains at different stages of magnetization. In the beginning, they are disoriented, and then gradually aligned with increasing magnetic field, finally misaligned again when moments cancel each other and yield zero net magnetic moment. For hysteresis loop measurement, we used an alternating gradient magnetometer (AGM). The samples were mounted at the end of a holder by vacuum grease, and subjected to a fixed direct current (DC) field with an alternating field gradient.

3.4 X-ray Powder Diffraction

X-ray powder diffraction (XRD) is an analytical technique mainly used for identifying a material's crystal structure and phase fraction[41,42]. The basic process for XRD can be described as three steps[36,37]. Firstly, X-rays are generated in cathode ray tube via heating a filament, then these X-rays are filtered by foils or crystal monochromators to produce monochromatic X-rays. Finally, these X-rays are collimated and directed to the sample. When the incident X-ray satisfies Bragg's Law, constructive interference leads to an observable intensity peak. A detector records this X-ray signal and counts the number of incoming X-rays at each angle. In this thesis, a PANalytical X'Pert diffractometer (Cu K α radiation, $\lambda=0.1541$ nm, 45 kV and 40 mA) was used for XRD characterization. Bragg's Law is a classic principle used for XRD, which gives the angle for coherent and incoherent scattering from a crystal lattice[43]. X-rays are scattered from lattice planes with interplanar spacing d , when the scattered waves interfere constructively, they remain in phase. It is because the path length of every wave is equal to an integer multiple of the wavelength, which can be expressed by the equation 4. Here λ represents the wavelength of X-rays, n is a positive integer, d represents interplanar spacing, and θ represents the diffraction angle.

$$n\lambda = 2d\sin\theta \quad (4)$$

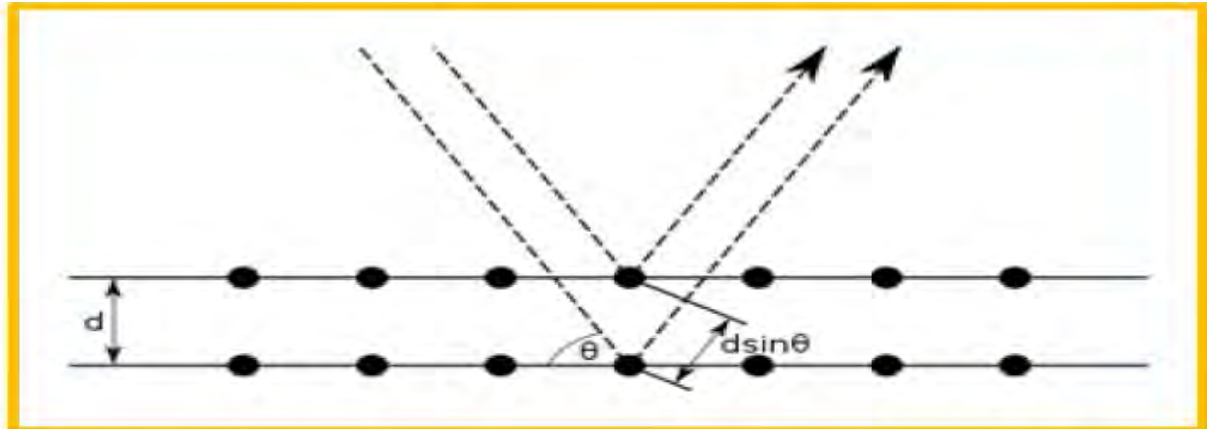


Figure 3.6. Bragg diffraction. Two beams with identical wavelength and phase approach a crystalline solid and are scattered off two different atoms within it. The lower beam traverses an extra length of $2d\sin\theta$. Constructive interference occurs when this length is equal to an integer multiple of the wavelength of the radiation[43].

3.5 Scanning Electron Microscopy

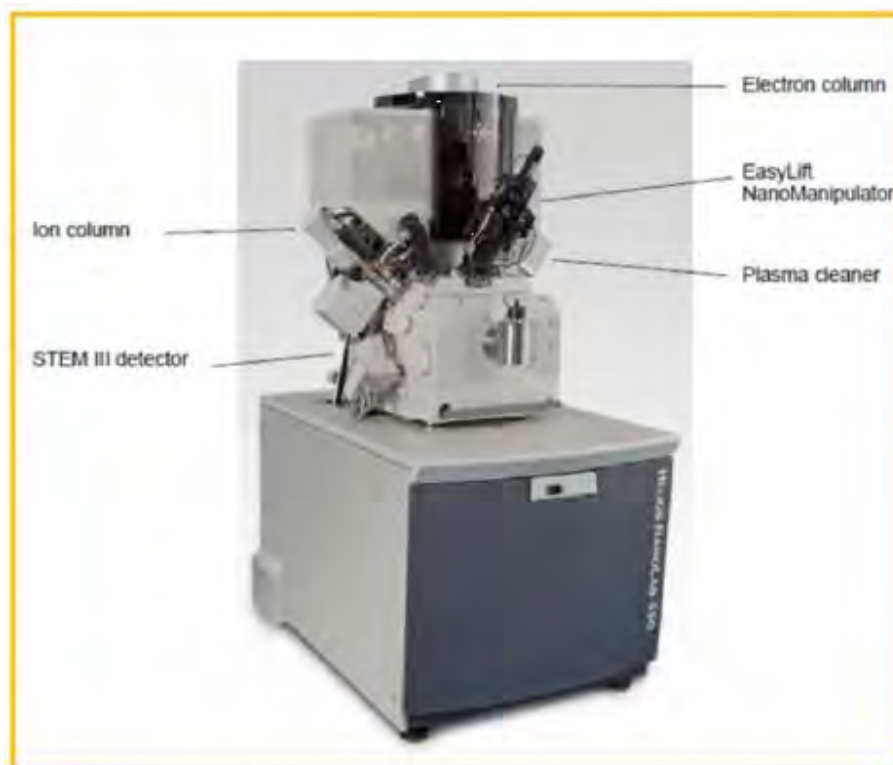


Fig.3.7 Scanning Electron Microscopy

3.6 Equipment needed for sample preparation and characterization.

The equipment needed to characterize and measure ALNICO 5 are Wayne kerr impedance analyzer ,Four point probe , VSM, Hall probe ,Magnetic coil ,XRD and FSEM. All these instrument are available at solid state physics lab ,dept of physics ,BUET Dhaka-1000.

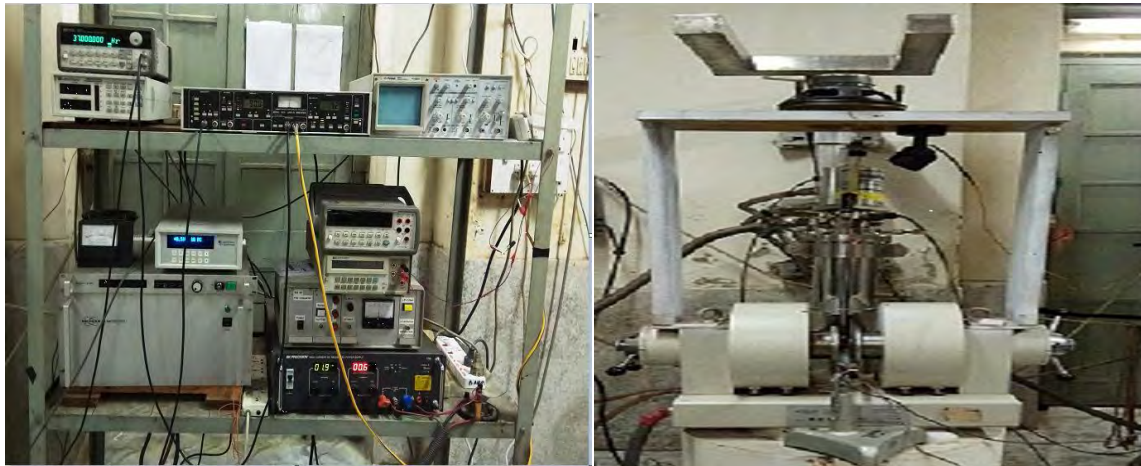


Fig.3.8 VSM measurement system



Fig. 3.9 magnetoresistance measurement system



Fig.3.10Wayne kerr impedance analyzer

References:

- [1] M. Tokushichi, "Magnet steel containing nickel and aluminum." Google Patents ,1938
- [2] E.-M. UK, "How Alnico Magnets are made," Alnico Specialists'. Tokushichi, "Strong permanent magnet with cobalt." Google Patents,14-Jan-1936.
- [3] K. Prange, "Alnico, the Miracle Metal," 2009.
- [4] A. S. Rao and D. Ph, "Alnico Permanent Magnets," vol. 62, no. 1949, pp. 373–383,1959.
- [5] E. R. Cronk, "Recent Developments in High-Energy Alnico Alloys," J. Appl.Phys., vol. 37, no. 3, p. 1097, 1966.
- [6] J. E. Gould, "Magnets with columnar crystallization," Cobalt & Cobalt Abstr, vol.23, pp. 82–87, 1964.
- [7] M. McCaig, "Recent developments in permanent magnetism," J. Appl. Phys., vol.35, no. 3, pp. 958–965, 1964.
- [8] A. Palasyuk, E. Blomberg, R. Prozorov, L. Yue, M. J. Kramer, R. W. McCallum, I.E. Anderson, and S. Constantinides, "Advances in characterization of non-rare-earth permanent magnets: Exploring commercial alnico grades 5-7 and 9,"Jom, vol. 65, no. 7, pp. 862–869, 2013.
- [9] L. Zhou, M. K. Miller, P. Lu, L. Ke, R. Skomski, H. Dillon, Q. Xing, A. Palasyuk,
- [10] M. R. McCartney, D. J. Smith, S. Constantinides, vol. 74, pp. 224–233, 2014.
- [11] W. Tang, L. Zhou, A. G. Kassen, A. Palasyuk, E. M. White, K. W. Dennis, M. J.Kramer, R. W. McCallum, and I. E. Anderson, "New alnico magnets fabricatedfrom pre-alloyed gas-atomized powder through diverse consolidation techniques,"Magn. IEEE Trans., vol. 51, no. 11, pp. 1–3, 2015.
- [12] I. E. Anderson, A. G. Kassen, E. M. H. White, L. Zhou, W. Tang, A. Palasyuk, K.W. Dennis, R. W. McCallum, and M. J. Kramer, "Novel pre-alloyed powderprocessing of modified alnico 8: Correlation of microstructure and magnetic properties," J. Appl. Phys., vol. 117, no. 17, p. 17D138, 2015.
- [13] Magnet Energy Corp, "PM history."
- [14] Y. Iwama and M. Takeuchi, "Spinodal Decomposition in Alnico 8 Magnet Alloy,Trans. J I M, vol. 15. pp. 371–377, 1974.

- [15] R. W. Balluffi, S. Allen, and W. C. Carter, *Kinetics of materials*. John Wiley & Sons, 2005.
- [16] D. A. Porter, K. E. Easterling, and M. Sherif, *Phase Transformations in Metals and Alloys*, (Revised Reprint). CRC press, 2009.
- [17] J. J. De Jong, J. M. G. Smeets, and H. B. Haanstra, "Some results of an electronmicroscopical study of the metallographic structure of two alloys for permanent magnets (Ticonal G and Ticonal X)," *J. Appl. Phys.*, vol. 29, no. 3, pp. 297–298, 1958.
- [18] G. Marcon, R. Peffen, and H. Lemaire, "A contribution to the study of Alnico 5 thermal treatment in magnetic field," *Magn. IEEE Trans.*, vol. 14, no. 5, pp. 688–689, 1978.
- [19] G. Begin and A. Dube, "Constitutional, morphological and magnetic properties of Alnico alloys," vol. 7, no. 1, pp. 35–39. Y. B. Kim, S. A. Song, and T. K. Kim, "Effects of the heat treatment on the microstructures and magnetic properties in Alnico 5," *Magn. IEEE Trans.*, vol. 23, no. 4, pp. 1952–1955, 1987.
- [20] H. M. Dillon, "Effects of heat treatment and modifications on microstructure in alnico," A. Hoffmann and H. StÄblein, "Investigations of high-coercivity alnico alloys," *Magn. IEEE Trans.*, vol. 6, no. 2, pp. 225–230, 1970.
- [21] W. G. Chu, W. D. Fei, X. H. Li, D. Z. Yang, and J. L. Wang, "Evolution of Fe-Co rich particles in Alnico 8 alloy thermo magnetically treated at 800C," *Mater. Sci. Technol.*, vol. 16, no. February, pp. 1023–1028, 2000.
- [22] B. G. Livshitz, B. A. Samarin, and V. S. Shubakov, "Features of the thermal magnetic treatment of diaconal 2000 type high-coercivity alloys," *Magn. IEEE Trans.*, vol. 6, no. 2, pp. 242–245, 1970.
- [23] C. A. Julien and F. G. Jones, "Alpha-Sub-Gamma Phase in Alnico 8 Alloys," *J. Appl. Phys.*, vol. 36, no. 3, pp. 1173–1174, 1965.
- [24] R. C. O'Handley, *Modern magnetic materials: principles and applications*, vol. 830622677. Wiley New York, 2000.
- [25] T. Liu, W. Li, M. Zhu, Z. Guo, and Y. Li, "Effect of Co on the thermal stability and magnetic properties of Alnico 8 alloys," *J. Appl. Phys.*, vol. 115, no. 17, pp. 34–37, 2014.
- [26] Y. Iwama, M. Inagaki, and T. Miyamoto, "Effects of Titanium in Alnico 8-Type Magnet Alloys," *Trans. Japan Inst. Met.*, vol. 11, no. 4, pp. 268–274, 1970.

- [27] M. Takeuchi and Y. Iwama, "Effects of Titanium upon Magnetic Anisotropy and Coercivity in Alnico Magnet Alloys," *Trans. Japan Inst. Met.*, vol. 17, no. 8, pp.489–496, 1976.
- [28] S. Szymura and S. Golba, "The influence of Niobium on the magnetic properties of the columnar Alnico 5 permanent magnets," *J. Magn. Magn. Mater.*, vol. 24, no.3, pp. 285–287, 1981.
- [29] M. Sugiyama and K. Shida, "The effect of the addition of niobium on sintered Alnico magnet properties.," *Trans. Japan Inst. Met.*, vol. 3, no. 2, 1962.
- [30] B. D. Cullity and C. D. Graham, *Introduction to magnetic materials*. John Wiley & Sons, 2011.
- [31] M. Durand-Charre, C. Bronner, and J.-P. Lagarde, "Relation between magnetic properties and crystallographic texture of columnar Alnico 8 permanent magnets," *Magn. IEEE Trans.*, vol. 14, no. 5, pp. 797–799, 1978.
- [32] N. Makino and Y. Kimura, "Effect of duplex addition of S and Te in the columnar alnico magnet alloys containing Ti," *Magn. IEEE Trans.*, vol. 6, no. 2, pp.302–303, 1970.
- [33] W. Wright and A. Thomas, "Influence de aluminum et du titane sur la structure de l'odification des alliages magnetiques du tupe Alnico," *Cobalt*, vol. 13, pp. 24–28, 1961.
- [34] A. I. Luteijn and K. J. de Vos, "Philips Res. Rept. 11, 489 (1956); AJJ Koch," in *MG van der Steeg, and KJ de Vos, Proc. AIEE Conf. Magnetism Magnetic Materials*, Boston, p. 173, 1956.
- [35] N. Makino and Y. Kimura, "Techniques to achieve texture in permanent magnet alloy systems," *J. Appl. Phys.*, vol. 36, no. 3, pp. 1185–1190, 1965.
- [36] Wikipedia, "Melt spinning."
- [37] W. D. Callister and D. G. Rethwisch, *Materials science and engineering: an introduction*, vol. 7. Wiley New York, 2007.
- [38] S. Dris, "Magnetic Hysteresis." ,2016.
- [39] B. Butrow and C. Clark, "X-ray Powder Diffraction (XRD)."
- [40] Bragg, W.H.; Bragg, W.L. "The Reflexion of X-rays by Crystals". *Proc R. Soc. Lond. A*. H. P. Myers (2002). *Introductory Solid State Physics*. Taylor & Francis..

Chapter four Spinodal decomposition

4.1 INTRODUCTION

Spinodal decomposition is a mechanism for the rapid unmixing of a mixture of liquids or solids from one thermodynamic phase, to form two coexisting phases. As an example, consider a hot mixture of water and an oil. At high temperatures the oil and the water may mix to form a single thermodynamic phase in which water molecules are surrounded by oil molecules and vice versa. The mixture is then suddenly cooled to a temperature at which thermodynamic equilibrium favors an oil-rich phase coexisting with a water-rich phase. Spinodal decomposition then occurs when the mixture is such that there is essentially no barrier to nucleation of the new oil-rich and water-rich phases. In other words, the oil and water molecules immediately start to cluster together into microscopic water-rich and oil-rich clusters throughout the liquid. These clusters then rapidly grow and coalesce until there is a single macroscopic oil-rich cluster, the oil-rich phase, and a single water-rich cluster, the water-rich phase.

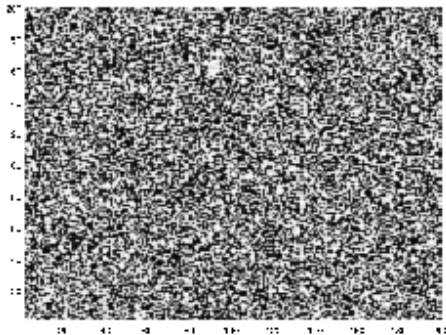
Spinodal decomposition can be contrasted with nucleation and growth. There the initial formation of the microscopic clusters involves a large free energy barrier, and so can be very slow, and may occur as little as once in the initial phase, not throughout the phase, as happens in spinodal decomposition.

Spinodal decomposition is of interest for two primary reasons. In the first place, it is one of the few phase transition in solids for which there is a complete quantitative theory. The reason for this is the inherent simplicity of the reaction. Since there is no thermodynamic barrier to the reaction inside of the spinodal region, the decomposition is determined solely by diffusion. Thus,

it can be treated purely as a diffusional problem, and many of the characteristics of the decomposition can be described by an approximate analytical solution to the general diffusion equation.

In contrast, theories of nucleation and growth have to invoke the thermodynamics of fluctuations. And the diffusional problem involved in the growth of the nucleus is far more difficult to solve, because it is unrealistic to linearize the diffusion equation.

From a more practical standpoint, spinodal decomposition provides a means of producing a very finely dispersed microstructure that can significantly enhance the physical properties of the material.



4.2 The Mechanism of Spinodal Decomposition

The spinodal is defined as the point where the curvature of the Gibbs free energy with respect to concentrations is zero, or:

$$d^2G/dc^2 = 0$$

[1]The condition for stability is that the curvature of the Gibb's free energy must be equal to or greater than zero; the unstable region is defined by the locus of the spinodal [1]. Above the spinodal region, or when the curvature of the Gibb's free energy is positive, the two phase region decomposes by nucleation and growth, and below this region, the two phase region decomposes by spinodal decomposition. A diagram of

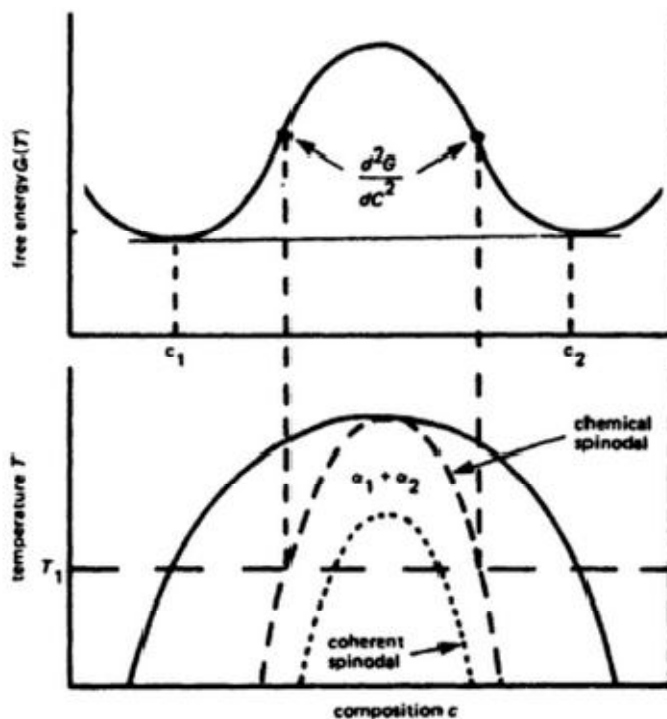


Figure 4.1: Variation of the chemical and coherent spinodal with composition. The region within which two phases are stable is called the miscibility gap [3]

the spinodal can be seen in Figure 21. A concentration gradient causes uphill diffusion, or diffusion in the direction against the gradient, if the composition is inside the spinodal, and downhill diffusion otherwise the change in free energy acts as the driving force for diffusion [2]. Spinodal decomposition is one mechanism by which an alloy decomposes into equilibrium phases. It was first proposed by Hillert's thesis in 1956 [2] as a method to explain the growth of a

composition modulation in an alloy that begins with a homogenous composition. Such a mechanism implies a negative diffusion coefficient. Hillert derived a new diffusion equation for cases where the third derivative of concentration is large; this equation accounts for the fact that a concentration gradient does not always cause downward diffusion. Hillert also developed a model from the zeros approximation of nearest-neighbor interactions. The model predicts the existence of periodically modulated structures in ordering, as well as in precipitation systems [4] by deriving an expression for the free energy of the system. A diffusion equation was also derived, which took into account the discontinuity in composition between planes in crystalline solids [4]. This model predicts the formation of many wavelengths during the first stage of transformation [4].

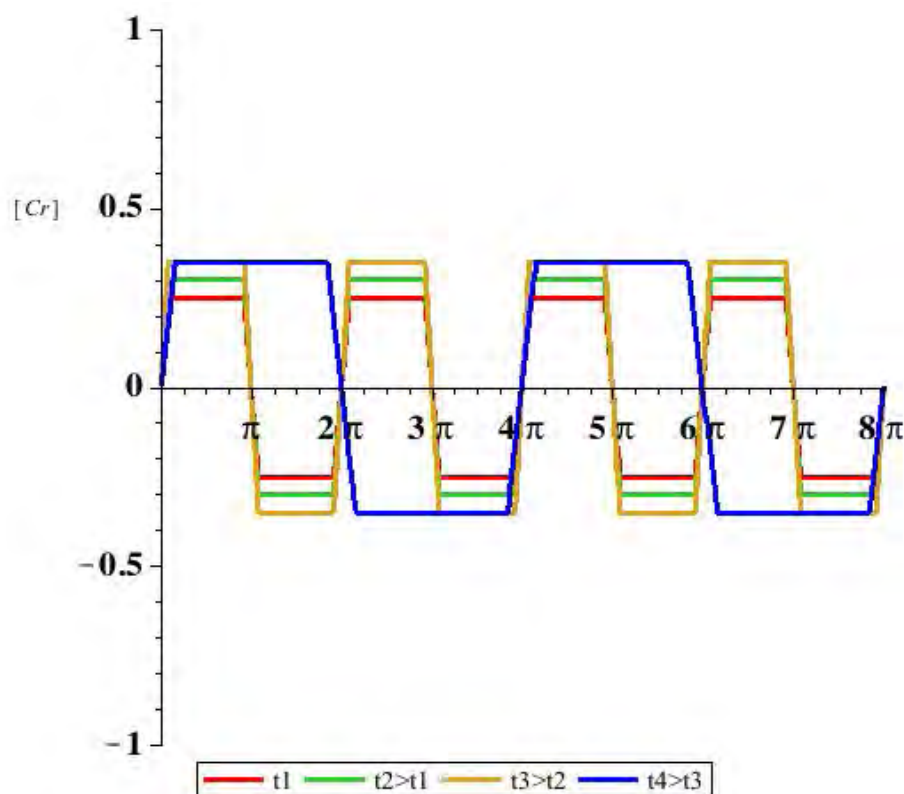


Figure 4.2: The progression of the sinusoidal composition profile through time. [8].

4.3 The Evolution of Concentration Profiles

During spinodal decomposition, the two phases separate from each other into a sinusoidal composition profile[5]. This takes place over two stages. First, a primary wavelength forms, and the difference in concentration between the two phases increases exponentially until the limit as set by the miscibility gap, or the two phase region where both phases are stable [6], is reached. If aging continues, the coarseness of the composition increases, but the concentration of each phase will be constant. The process is illustrated in Figure 22. This results in a sinusoidal composition profile, with a wavelength of approximately five nm or less [7].

Cahn determined that true spinodal decomposition possesses two properties. It occurs everywhere within the sample, with the exception of near structural imperfections where the rate or mechanism may be different, and the amplitude of composition fluctuations should grow continuously until a metastable equilibrium is reached, with a preferential amplification of certain wavelength components [1].

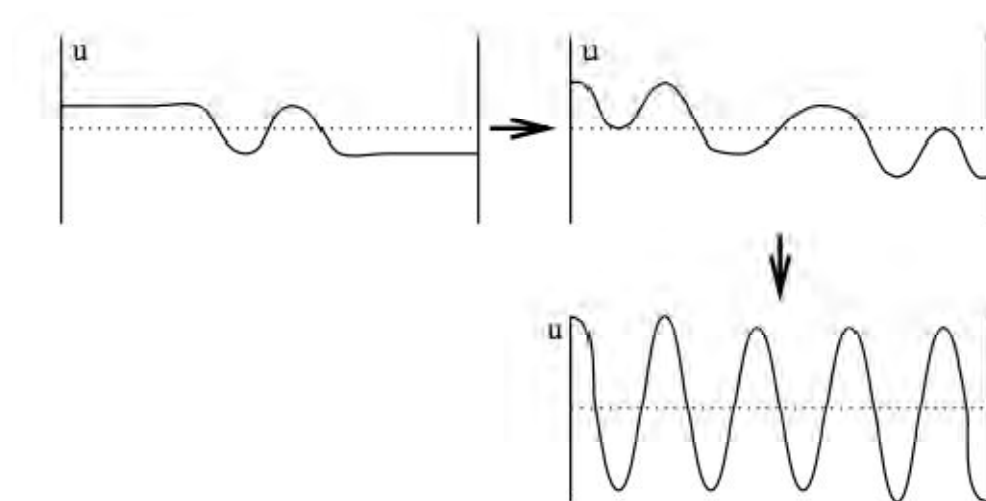


Figure 4.3: A typical evolution sequence for the Cahn-Hilliard equation, where u represents the concentration. As time progresses the concentration approaches a sinusoidal composition profile, as that of spinodal decomposition. [10].

4.4 The Cahn-Hilliard Equation

Cahn and Hilliard determined a governing equation to describe the process of phase separation:

$$\frac{dc}{dt} = D\nabla^2(c^3 - c - \gamma\nabla^2c)$$

[9]where D is the diffusion coefficient, c is the concentration, and γ is the surface energy. If a linear analysis of the Cahn-Hilliard equation is performed, it suggests that spinodal decomposition occurs [10]. A typical evolution sequence can be seen in Figure 23. As time progresses, the concentration approaches a sinusoidal composition profile, as that of spinodal decomposition.

An example of a numerical solution to the Cahn-Hilliard equation can be seen in Figure 24. The solution begins at an unstable concentration (a), and decomposes into two distinct phases with a characteristic length scale (through c). As time continues to progress, the length scale is coarsened while maintaining fixed phase concentration fractions [11].

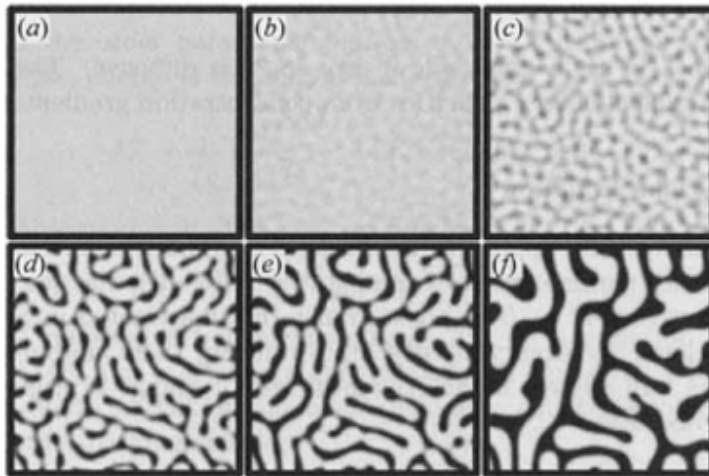


Figure 4.4: A numerical solution to the Cahn-Hilliard equation, demonstrating spinodal decomposition. The system begins at an unstable concentration (a), and decomposes into two distinct phases with a characteristic length scale (b, c); as time progresses, the length scale coarsens while maintaining fixed phase concentration fractions.

The initial stage composition can be expressed by the equation:

$$X - X_s = A \cos(\beta X)$$

[12], where A is the amplitude of the fluctuating wave, and

The critical wavelength is given by:

$$\lambda_c = \left(\frac{-8\pi^2 \kappa}{d^2G/dX^2} \right)^{1/2}$$

[12], where κ is a materials constant known as the gradient energy coefficient. All wavelengths longer than this critical wavelength are unstable, and will amplify to trigger the spinodal decomposition process. For a one-dimensional system, the solution to the Cahn-Hilliard equation takes the form:

$$c - \langle c \rangle = e^{R(\beta)t} \cos(\beta x)$$

where $R(\beta)$ is the amplification factor [12]. The amplification factor can be plotted as a function of wavenumber or wavelength, to predict the wavelength that grows most rapidly with time.

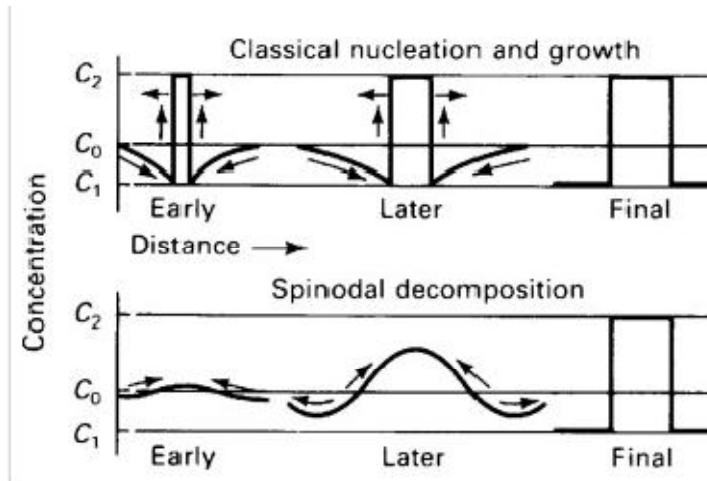


Figure 4.5: The sequences of formation of a two-phase mixture by nucleation and growth (above) and spinodal decomposition [13]

4.5 Spinodial Decomposition vs. Nucleation and Growth

Nucleation and growth is another method of decomposition into equilibrium phases; it occurs in the two-phase region when the curvature of the Gibb's free energy is positive, or above the spinodal. Nucleation thus occurs in the metastable region of the phase diagram [11]. The system initiates a discontinuous phase transformation, as seen in Figure 25. Nucleation requires localized fluctuations in composition that are large enough that the free energy decreases from the chemical driving force, enough to offset all terms that resist the transformation, such as the elastic strain energy. The transformation begins at discrete nucleation sites, and evolves by outward growth of the nuclei of the new phase, as seen in Figure 25. Nucleation and growth can thus be categorized as a "discontinuous" phase transformation, where spinodal decomposition is a "continuous" phase transformation. This distinction occurs as spinodal decomposition arises from systems that are thermodynamically unstable, as is indicated by the curvature of the Gibb's free energy, where nucleation and growth occurs in metastable systems [11]. The evolution of the phase separation differs between the two processes. The second-phase structure that evolves by nucleation and growth results in more spherical nuclei, where spinodal decomposition has a worm-like or tweed-like interconnectivity [12].

4.6 Coherency strains

For most crystalline solid solutions, there is a variation of lattice parameter with composition. If the lattice of such a solution is to remain coherent in the presence of a composition modulation, mechanical work has to be done in order to strain the rigid lattice structure. The maintenance of coherency thus affects the driving force for diffusion.

Consider a crystalline solid containing a one-dimensional composition modulation along the x-direction. We calculate the elastic strain energy for a cubic crystal by estimating the work required to deform a slice of material so that it can be added coherently to an existing slab of cross-sectional area. We will assume that the composition modulation is along the x' direction and, as indicated, a prime will be used to distinguish the reference axes from the standard axes of a cubic system (that is, along the <100>).

Let the lattice spacing in the plane of the slab be a_0 and that of the unreformed slice a . If the slice is to be coherent after addition of the slab, it must be subjected to a strain ϵ in the z' and y' directions which is given by:

$$\epsilon = \frac{a - a_0}{a_0}$$

In the first step, the slice is deformed hydrostatically in order to produce the required strains to the z' and y' directions. We use the linear compressibility of a cubic system $1 / (c_{11} + 2c_{12})$ where the c's are the elastic constants. The stresses required to produce a hydrostatic strain of δ are therefore given by:

$$\sigma_{x'} = \sigma_{y'} = \sigma_{z'}$$

The elastic work per unit volume is given by:

$$W_E = \frac{1}{2} \sum_i \sigma_i \epsilon_i$$

where the ϵ 's are the strains. The work performed per unit volume of the slice during the first step is therefore given by:

$$W_E(1) = \frac{3}{2}(c_{11} + 2c_{12})\sigma^2$$

In the second step, the sides of the slice parallel to the x' direction are clamped and the stress in this direction is relaxed reversibly. Thus, $\varepsilon_{z'} = \varepsilon_{y'} = 0$. The result is that:

$$W_E(2) = \frac{\sigma^2(c_{11} + 2c_{22})}{2c_{11}}$$

The net work performed on the slice in order to achieve coherency is given by:

$$W_E = W_E(1) - W_E(2)$$

or

$$W_E = \left(\frac{\sigma^2}{2}\right)(c_{11} + 2c_{12}) \left(3 - \left[\frac{c_{11} - 2c_{12}}{c_{1'1'}}\right]\right)$$

The final step is to express $c_{1'1'}$ in terms of the constants referred to the standard axes. From the rotation of axes, we obtain the following:

$$c_{1'1'} = c_{11} + 2(2c_{44} - c_{11} + c_{12})(l^2m^2 + m^2n^2 + l^2n^2)$$

where l, m, n are the direction cosines of the x' axis and, therefore the direction cosines of the composition modulation. Combining these, we obtain the following

$$W_E = Y\sigma^2$$

$$Y = \frac{1}{2}(c_{11} + 2c_{12}) \left[3 - \frac{c_{11} + 2c_{12}}{c_{11} + 2(2c_{44} - c_{11} + c_{12})(l^2m^2 + m^2n^2 + l^2n^2)}\right]$$

The existence of any shear strain has not been accounted for. Cahn considered this problem, and concluded that shear would be absent for modulations along $\langle 100 \rangle$, $\langle 110 \rangle$, $\langle 111 \rangle$ and that for

other directions the effect of shear strains would be small. It then follows that the total elastic strain energy of a slab of cross-sectional area A is given by:

$$W_E = 4 \int Y \sigma^2 dx$$

We next have to relate the strain δ to the composition variation. Let a_0 be the lattice parameter of the unstrained solid of the average composition c_0 . Using a Taylor's series expansion about c_0 yields the following

$$a = a_0 [1 + \eta[c - c_0] + \dots]$$

in which

$$\eta = \left(\frac{1}{a_0} \right) \left(\frac{da}{dc} \right) + \frac{d \ln a}{dc}$$

where the derivatives are evaluated at c_0 . Thus, neglecting higher order terms, we have:

$$\sigma = \frac{a - a_0}{a_0} = \eta(c - c_0)$$

Substituting, we obtain:

$$W_E = A \int \eta^2 Y (c - c_0)^2 dx$$

his simple result indicates that the strain energy of a composition modulation depends only on the amplitude and is independent of the wavelength. For a given amplitude, the strain energy W_E is proportional to Y . Let us consider a few special cases.

For an isotropic material:

$$2c_{44} - c_{11} + c_{12}$$

so that:

$$Y[\text{iso}] = c_{11} + c_{12} - 2\left(\frac{c_{12}^2}{c_{11}}\right)$$

Thus equation can also be written in terms of Young's modulus E and Poisson's ratio ν using the standard relationships

$$c_{11} = \frac{E(1 - \nu)}{(1 - 2\nu)(1 + \nu)}$$

$$c_{12} = \frac{E\nu}{(1 - 2\nu)(1 + \nu)}$$

Substituting, we obtain the following:

$$Y[\text{iso}] = \frac{E}{1 - \nu}$$

For most metals, the left hand side of this equation

$$2c_{44} - c_{11} + c_{12}$$

is positive, so that the elastic energy will be a minimum for those directions that minimize the term: $l^2m^2 + m^2n^2 + l^2n^2$. By inspection, those are seen to be $\langle 100 \rangle$. For this case:

$$Y[100] = c_{11} + c_{12} - 2\left(\frac{c_{12}^2}{c_{11}}\right)$$

the same as for an isotropic material. At least one metal (molybdenum) has an anisotropy of opposite sign. In this case, the directions for minimum W_E will be those that maximize the directional cosine function. These directions are $\langle 111 \rangle$, and

$$Y[111] = \frac{6c_{44}(c_{11} + 2c_{12})}{c_{11} + 2c_{12} + 4c_{44}}$$

As we will see, the growth rate of the modulations will be a maximum in the directions that minimize Y . These directions therefore determine the morphology and structural characteristics of the decomposition in cubic solid solutions.

Rewriting the diffusion equation and including the term derived for the elastic energy yields the following:

$$F_t = A \int f(c) + \eta Y (c - c_0)^2 + K \left(\frac{dc}{dx} \right)^2 dx$$

or

$$\frac{\partial c}{\partial t} = \left(\frac{M}{N_\nu} \right) \left([f'' + 2\eta Y] \left(\frac{d^2 c}{dx^2} \right) - 2K \left(\frac{d^4 c}{dx^4} \right) \right)$$

which can alternatively be written in terms of the diffusion coefficient D as:

$$\frac{\partial c}{\partial t} = \left(\left[1 + \frac{2\eta Y}{f''} \right] \frac{d^2 c}{dx^2} - \frac{2KF}{f''} \frac{d^4 c}{dx^4} \right)$$

The simplest way of solving this equation is by using the method of Fourier transforms.

4.7 Fourier transform

The motivation for the Fourier transform comes from the study of a Fourier series. In the study of a Fourier series, complicated periodic functions are written as the sum of simple waves mathematically represented by sines and cosines. Due to the properties of sine and cosine it is possible to recover the amount of each wave in the sum by an integral. In many cases it is desirable to use Euler's formula, which states that $e^{2\pi i\theta} = \cos 2\pi\theta + i \sin 2\pi\theta$, to write Fourier series in terms of the basic waves $e^{2\pi i\theta}$, with the distinct advantage of simplifying many unwieldy formulas.

The passage from sines and cosines to complex exponentials makes it necessary for the Fourier coefficients to be complex valued. The usual interpretation of this complex number is that it gives you both the amplitude (or size) of the wave present in the function and the phase (or the initial angle) of the wave. This passage also introduces the need for negative "frequencies". (E.G. If θ were measured in seconds then the waves $e^{2\pi i\theta}$ and $e^{-2\pi i\theta}$ would both complete one cycle per second—but they represent different frequencies in the Fourier transform. Hence, frequency no longer measures the number of cycles per unit time, but is closely related.)

If $A(\beta)$ is the amplitude of a Fourier component of wavelength λ and wave number $\beta = 2\pi/\lambda$ the spatial variation in composition can be expressed by the Fourier integral:

$$c - c_0 = \int A(\beta) \exp(i\beta x) d\beta$$

in which the coefficients are defined by the inverse relationship:

$$A(\beta) = \frac{1}{2\pi} \int (c - c_0) \exp(-i\beta x) dx$$

Substituting, we obtain on equating coefficients:

$$\frac{dA(\beta)}{dt} = -\frac{M}{N_\nu} [f'' + 2\eta^2 Y + 2Y\beta^2] \beta^2 A(\beta)$$

This is an ordinary differential equation that has the solution:

$$A(\beta, t) = A(\beta, 0) \exp[R(\beta)t]$$

in which $A(\beta)$ is the initial amplitude of the Fourier component of wave wave number β and $R(\beta)$ defined by:

$$R(\beta) = -\frac{M}{N_\nu} (f'' + 2\eta Y + 2k\beta^2) \beta^2$$

or, expressed in terms of the diffusion coefficient D :

$$R(\beta) = -\bar{D} \left(1 + \frac{2\eta^2 Y}{f''} + \frac{2K}{f''} \beta^2 \right) \beta^2$$

In a similar manner, the new diffusion equation:

$$\frac{\partial c}{\partial t} = M \frac{\partial^2 f}{\partial c^2} \nabla^2 c - 2MK \nabla^4 c$$

has a simple sine wave solution given by:

$$c - c_0 = \exp[R\bar{\beta}t] \cos \beta \cdot r$$

where $R(\bar{\beta})$ is obtained by substituting this solution back into the diffusion equation as follows

$$R(\bar{\beta}) = M\beta^2 \left(\frac{\partial^2 f}{\partial c^2} + 2K\beta^2 \right)$$

For solids, the elastic strains resulting from (in)coherency add terms to the amplification factor $R(\beta)$ as follows

$$R(\bar{\beta}) = -M\beta^2 \left(\frac{\partial^2 f}{\partial c^2} + 2\eta^2 Y + 2K\beta^2 \right)$$

where, for isotropic solids:

$$Y = \frac{E}{1 - \nu}$$

where E is Young's modulus of elasticity, ν is Poisson's ratio, and η is the linear strain per unit composition difference. For anisotropic solids, the elastic term depends on direction in a manner which can be predicted by elastic constants and how the lattice parameters vary with composition. For the cubic case, Y is a minimum for either (100) or (111) directions, depending only on the sign of the elastic anisotropy

Thus, by describing any composition fluctuation in terms of its Fourier components, Cahn showed that a solution would be unstable with respect to sinusoidal fluctuations of a critical wavelength. By relating the elastic strain energy to the amplitudes of such fluctuations, he formalized the wavelength or frequency dependence of the growth of such fluctuations, and thus introduced the principle of selective amplification of Fourier components of certain wavelengths. The treatment yields the expected mean particle size or wavelength of the most rapidly growing fluctuation.

Thus, the amplitude of composition fluctuations should grow continuously until a metastable equilibrium is reached with a preferential amplification of components of particular wavelengths.

The kinetic amplification factor R is negative when the solution is stable to the fluctuation, zero

at the critical wavelength, and positive for longer wavelengths—exhibiting a maximum at exactly $\sqrt{2}$ times the critical wavelength.

Consider a homogeneous solution within the spinodal. It will initially have a certain amount of fluctuation from the average composition which may be written as a Fourier integral. Each Fourier component of that fluctuation will grow or diminish according to its wavelength.

Because of the maximum in R as a function of wavelength, those components of the fluctuation with $\sqrt{2}$ times the critical wavelength will grow fastest and will dominate. This "principle of selective amplification" depends on the initial presence of these wavelengths but does not critically depend on their exact amplitude relative to other wavelengths (if the time is large compared with $(1/R)$). It does not depend on any additional assumptions, since different wavelengths can coexist and do not interfere with one another.

Limitations of this theory would appear to arise from this assumption and the absence of an expression formulated to account for irreversible processes during phase separation which may be associated with internal friction and entropy production. In practice, frictional damping is generally present and some of the energy is transformed into thermal energy. Thus, the amplitude and intensity of a one-dimensional wave decreases with distance from the source, and for a three-dimensional wave the decrease will be greater.

4.8 Dynamics in k-space

In the spinodal region of the phase diagram, the free-energy can be lowered by allowing the components to separate, thus increasing the relative concentration of a component material in a particular region of the material. The concentration will continue to increase until the material reaches the stable part of the phase diagram. Very large regions of material will change their concentration slowly due to the amount of material which must be moved. Very small regions will shrink away due to the energy cost in maintaining an interface between two dissimilar component materials.

To initiate a homogeneous quench a control parameter, such as temperature, is abruptly and globally changed. For a binary mixture of A-type and B -type materials, the Landau free-energy

$$F = \int \left(\frac{A}{2} \phi^2 + \frac{B}{4} \phi^4 + \frac{\kappa}{2} (\nabla \phi)^2 \right) dx .$$

is a good approximation of the free-energy near the **critical point** and is often used to study homogeneous quenches. The mixture concentration $\phi = \rho_A - \rho_B$ is the density difference of the mixture components, the control parameters which determine the stability of the mixture are A and B, and the interfacial energy cost is determined by K .

Diffusive motion often dominates at the length-scale of spinodal decomposition. The equation of motion for a diffusive system is

$$\partial_t \phi = \nabla(m \nabla \mu + \xi(x)) ,$$

$\langle \xi(x) \rangle = 0$, and the chemical potential μ is derived from the Landau free-energy:

$$\mu = \frac{\delta F}{\delta \phi} = A\phi + B\phi^3 - \kappa \nabla^2 \phi .$$

$$\partial_t \bar{\phi}(k, t) = -m((A + 3B\phi_{in}^2)k^2 + \kappa k^4) \bar{\phi}(k, t) = R(k) \bar{\phi}(k, t) ,$$

which has an exponential growth solution:

$$\bar{\phi}(k, t) = \exp(R(k)t) .$$

Since the growth rate $R(k)$ is exponential, the fastest growing angular wavenumber

$$k_{sp} = \sqrt{\frac{-(A + 3B\phi_{in}^2)}{2\kappa}} ,$$

will quickly dominate the morphology. We now see that spinodal decomposition results in domains of the characteristic length scale called the spinodal length:

$$\lambda_{sp} = \frac{2\pi}{k_{sp}} = 2\pi \sqrt{\frac{2\kappa}{-(A + 3B\phi_{in}^2)}} .$$

The growth rate of the fastest growing angular wave number is

$$R(k_{sp}) = -m((A + 3B\phi_{in}^2)k_{sp}^2 + \kappa k_{sp}^4) = \frac{m(A + 3B\phi_{in}^2)^2}{4\kappa} = \frac{1}{t_{sp}}$$

where t_{sp} is known as the *spinodal time*.

The spinodal length and spinodal time can be used to non dimensionalize the equation of motion, resulting in universal scaling for spinodal decomposition.

References

- [1] J.W. Cahn. On spinodal decomposition. *Acta Metallurgica*, 9:795–801, 1961.
- [2] M. Hillert. A Theory of Nucleation for Solid Metallic Solutions. *Praca doktorska, of Technology*, 1954.
- [3] R.J. Bishop R.E. Smallman. *Modern Physical Metallurgy & Materials Engineering*. Butterworth-Heinemann, 1999.
- [4] M. Hillert. A solid-solution model for inhomogeneous systems. *Acta Metallurgica*, 9:525–535, 1961.
- [5] W.C. Carter R.W. Balluffi, S. Allen. *Kinetics of Materials*. John Wiley & Sons, 2005.
- [6] R.E. Reed-Hill R. Abbaschian, L. Abbaschian. *Physical Metallurgy Principles*. Cengage Learning, 2008.
- [7] M.K. Miller et al. Spinodal decomposition in fe-cr alloys: Experimental study at the atomic level and comparison with computer models - i. introduction and methodology. *Acta M*, 1995:3385–3401, 43.
- [8] W.C. Carter. Thermodynamics of materials, lecture 32 notes. MIT Open Courseware, 2002.
- [9] J.E. Hilliard J.W. Cahn. Free energy of a no uniform system. i. interfacial free energy. *Journal of Chemical Physics*, 28:258–267, 1958.
- [10] C.P. Grant. Spinodal decomposition for the cahn-hilliard equation. *Communications in Partial Differential Equations*, 18:453–490, 1993.
- [11] S. Puri. *Kinetics of Phase Transitions*. CRC Press, 2009.
- [12] S.H. Risbud. *Materials Processing Handbook*, Chapter 4. CRC Press, 2007.
- [13] F. Findik. Improvements in Spinodal Alloys from Past to Present. *Materials & Design*, 42:131–146, 2012.
- [14] J.W. Cahn. On spinodal decomposition in cubic crystals. *Acta Metallurgica*, 10:179–183, 1962.
- [15] M.R. da Silva J.M. Neto S. Pairis S.S.M. Tavares, R.F. de Noronha. 475C Embrittlement in a Duplex Stainless Steel UNS S31803. *Materials Research*, 4, 2001.

- [16] T.R. Lucas. The Effect of Thermal Aging and Boiling Water Reactor Environment on Type 316L Stainless Steel Welds. Praca doktorska, Massachusetts Institute of Technology, 2011.
- [17] H.M. Chung, O.K. Chopra. Kinetics and Mechanism of Thermal Aging Embrittlement of Duplex Stainless Steels. June 1987.
- [18] R.G. Ballinger J.H. Kim. Stress Corrosion Cracking Crack Growth Behavior of Type 316L Stainless Steel Weld Metals in Boiling Water Reactor Environments. NACE, 2008.
- [19] M.U. Kim et. al. Application of spinodal decomposition to produce metallic glass matrix composite with simultaneous improvement of strength and plasticity. *Met. Mater. Int.*, 15:193–196, 2009.

Chapter Five

RESULTS AND DISCUSSIONS

5.1 Introduction

In this work we have investigated the effect of heat treatment on the dc and ac magnetic properties of Alnico V ribbon samples. The structural analysis have convincingly proven that the alloy has a crystalline state even in its ribbon form . Fig5.4(a) shows the X-ray diffraction of the Alnico V . The intensity versus 2 Theta curve shows sharp crystalline peaks . Also the peak positions indictate that the alloy maintains the pure bcc structure which is magnetic. All the as made samples regardless of the wheel speed has shown pure crystallinity and magnetic in nature and there is no trace of any glassy phase in all the studied samples. However controlled heat treatment has nucleated some mixed crystalline and glassy phase. This is attributed to the aging process of the ribbons. After long exposure to the aging process at 900C followed by 600C it is assumed that some pockets of glassy phase has evolved in the sample but still largely maintaining the crystalline states. This mixed phase has a clear effect on the anomalous magneto resistive behavior of the sample. The magneto-resistance of the heat treated sample has deviated significantly from that of the as made sample. In certain shape memory alloy a significant anomaly is observed in the magneto-resistive behavior. A sudden jump (magneto-resistive jump) is observed in the magneto resistance as the magnetic field is swept from positive magnetic field to the negative maximum field. It is still premature to level this magneto-resistive behavior in Alnico V ribbons as a signature of shape memory alloy. However we found some

similarity in this regard which needs further investigations. To investigate the effect of small amount of Boron in the alloy 2 wt% Boron was added using plasma arc melting . The saturation magnetization is slightly reduced after B addition although there is no observed boride phase after the addition of B in the alloy. The XRD of the ribbon with Boron addition is shown in Fig.5.4(b). The addition of B has only improved the elastic properties e.g., ductility of the alloy as fabrication of the ribbons were easier after adding the trace amount of Boron.

5.2 surface morphology of alnico v

SEM images of as-spun (25 and 50 m/s) and heat-treated samples at 900 °C for 30 min and aged at 600 °C for 4 hours are shown in figure 5.2(a) ,5,3(b) and 5.3(c). By examining SEM images of several different regions of the ribbons a drastic reduction of the grain size is clearly visible, from 1-10 μm to roughly 1 μm and below in the samples produced at 25 m/s and 50 m/s copper wheel speed, respectively. After the heat treatment to induce the spinodal decomposition the grain size is almost doubled to around 10 μm and 1 μm in the ribbons produced at 25 m/s and 50 m/s, respectively. The developed spinodal structures within the grains are shown in the high-resolution SEM images (figure 5.2(c) , bottom).

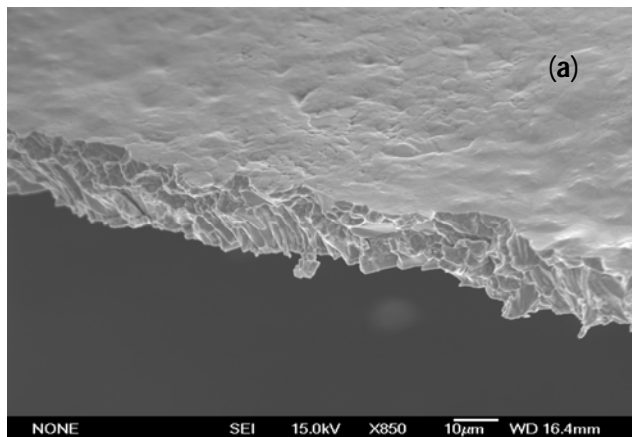


Fig.5.2(a):SEM showing equiaxed grains cross-sectional structures

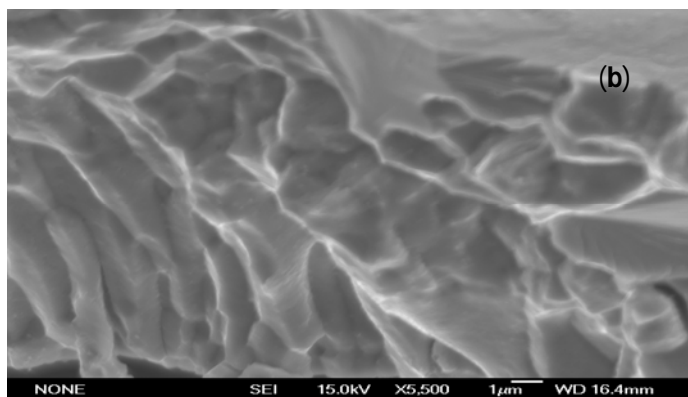


Fig.5.2(b):As made ribbon SEM image shows equi-axed shaped grains

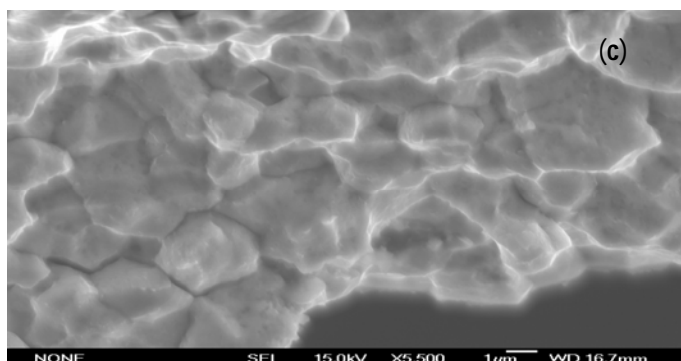


Fig.5.2(c): Annealing followed by aging has drastically changed the microstructure

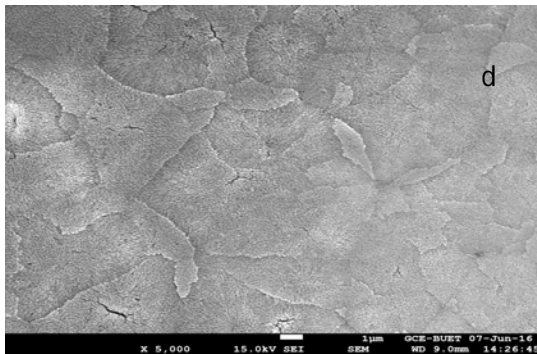


Fig . 5.2 (d): FESEM image ($\times 5$ k) of 25 ms^{-1} alnico v

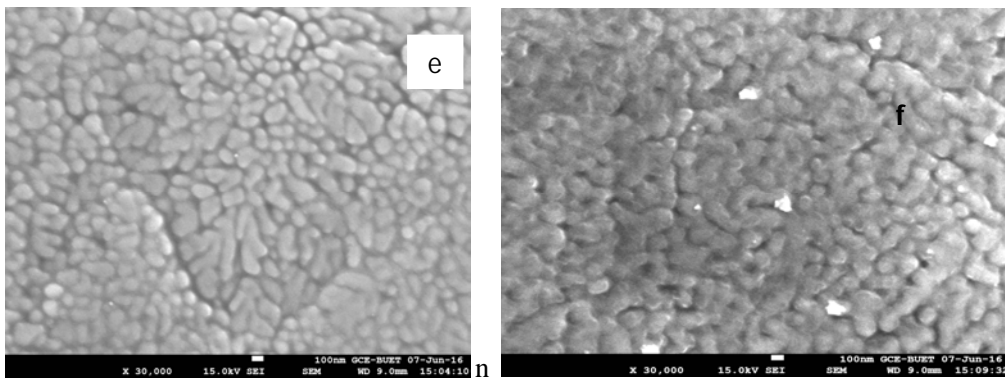


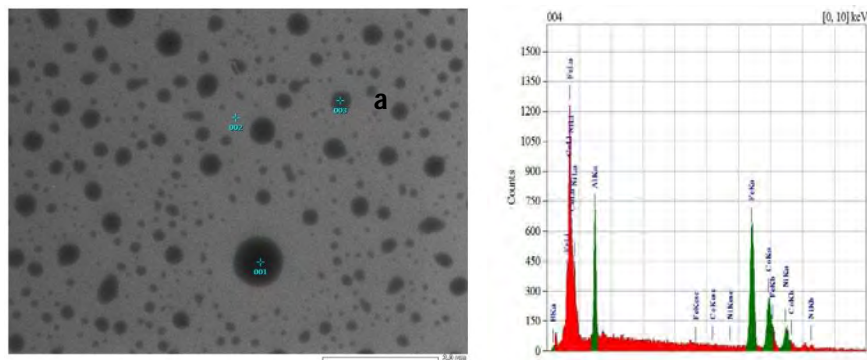
Fig. 5.2(e): FESEM image ($\times 30$ k) of 50 ms^{-1} of alnico v .(f) After heat treatment

Fig.5.2 (d) shows the Field effect Scanning Electron Microscopic image of Alnico V ribbon melt spun at 25 m/sec . The surface morphology shows well defined but randomly distributed grain boundaries. These boundaries were created during the rapid quenching after being injected on the fast spinning wheel.

Fig.5.2(e) shows A typical interpenetrating block structure is observed in our samples, which is in contrast to the work by Akdogan et al. on Alnico thin films [1]. The brighter block like shapes correspond to Fe Co -rich α_1 phase and the dark interspersing phase represents the $AlNi$ -rich α_2 phase. The spinodal structures have approximately the same size in both samples. It can be concluded that grain sizes in the range of several micrometers have only a weak influence on the morphology of the spinodal structures. The grain size of Alnico ribbons was decreased by an

order of magnitude by increasing the copper wheel speed from 25 m/s to 50 m/s to values, from 10 μm to about 1 μm . The ribbons with bigger grains have a slightly finer spinodal morphology than the smaller grained ribbons, although the difference is not pronounced. It seems that in the range of μm the grain size does not strongly influence the size of the spinodal structures.

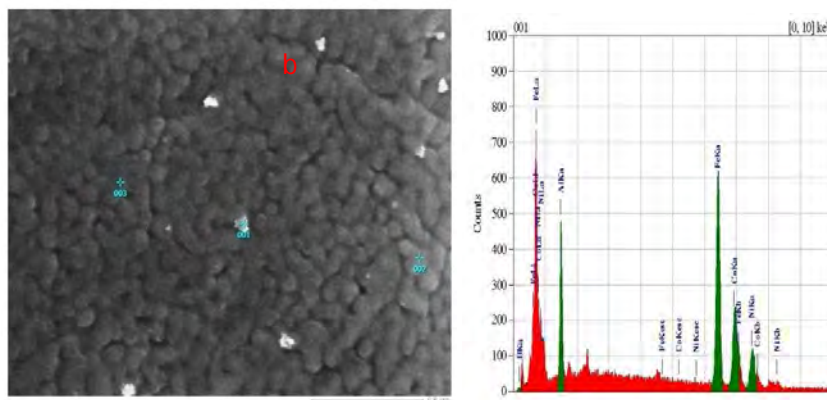
5.3 Elemental analysis



Element	(keV)	Mass%	Sigma	Atom%
B K	*			
Al K	1.486	10.37	0.19	19.67
Fe K	6.398	51.84	0.67	47.49
Co K	6.924	23.28	0.54	20.21
Ni K	7.471	14.50	0.49	12.64
Total		100.00		100.00

Fig. 5.3(a): EDX spectrum of 25 ms^{-1}

The EDX analysis of as made alnico v ribbon at 25 m/s sample Fig. 5.3(a) confirms that we get our desire elements. The percentage of atoms are Al 19.67 ,Fe 47.49, Co 20.21 and Ni 12.64 percent .Here the speed of copper wheel at 25 m/s. The EDX shows there is no impurity .We do not found any Boron addition in our sample.



Element	(keV)	Mass%	Sigma	Atom%
B K *				
Al K	1.486	7.61	0.11	14.84
Fe K	6.398	53.59	0.32	50.48
Co K	6.924	23.60	0.31	21.07
Ni K	7.471	15.20	0.31	13.62
Total		100.00		100.00

Fig 5.3 (b) : EDX spectrum of 50 ms⁻¹

It is seen from the EDX Fig. 5.3 (b) the percentage of atoms are Al 14.84% , Fe 50.48%, Co 21.07% and Ni 13.62% which confirms our desire composition .Data of elemental analysis for prepared ribbon the EDX reveals that the highest value of Fe atomic percentage is 50 .48 for 51 at % Fe.The prominent percentage of Co 21.07% for 24 at % Co and the other atomic percent is such as Al 14.84% instead of 8% Al. Finally we found there is no impurity in our stoichiometric.

The EDX confirms the composition of the constituent elements present in the samples. There is no any impurities index in the compounds. EDX spectroscopy also confirmed the homogeneous distribution of the constituent elements. It is observed from the EDX spectrum that the percentage of the element in the component is well consistent in ribbon form. the EDX analysis shows there is no boron in ribbon form at various speed.

5.4 X-ray Diffraction of melt spun Alnico V ribbon

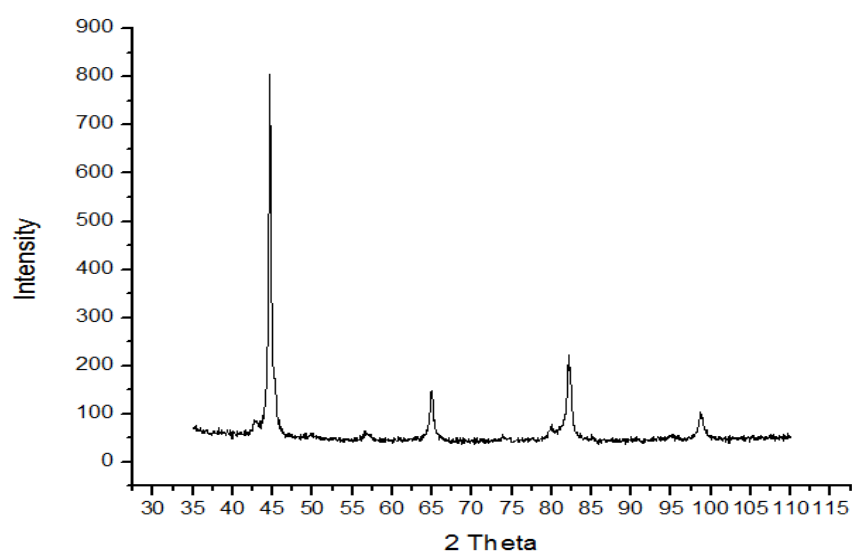


Fig.5.4(a) XRD patterns of alnico V ribbon.

All the as made and annealed samples Fig.5.4 (a) show pure crystalline structure as revealed by the X-ray Diffraction analysis unlike most of the iron, cobalt and nickel based ribbons which show amorphous or glassy structure after melt-spinning. The sharp peak confirms that the ribbons are crystalline(pure bcc). We find the peak at 45°angle is very sharp and other peak at

82.5° angle. The Intensity of the first peak is around 800 a.u. the other peak of the Intensity at 82.5 degree is 200 a. u.

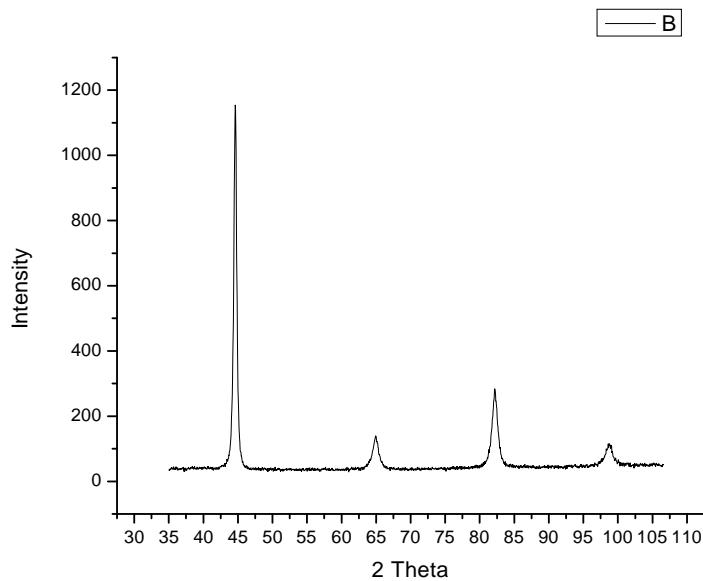


Fig.5.4(b)X-ray Diffraction of Alnico V with B addition

We show another Fig.5.4 (b) X –ray analysis of Alnico V with Boron addition. We find some difference in intensity but the peak is almost the same. The addition of Boron the X-ray Fig. 5.4 (b) the intensity is around 1200 a.u and the other sharp peak of intensity is around 300 a.u.The grain size decreased significantly with B addition .Because addition of B a minor secondary phase is formed then the grain size was decreased by B addition, a significantly finer spinodal structure developed compared to samples without B [2].

5.5 Effect of mechanical alloying on the magnetic properties

Hysteresis loops for the mechanically alloyed ALNICO V samples are shown in Figure 5.1. The magnetization curves show typical soft magnetic behavior with low coercivity. The magnetic properties of Alnico v sample has been determined at room temperature at (300K) using a vibrating sample magnetometer (VSM).

The hysteresis loop begins at a starting point with zero applied field ($H=0$), at this state, all the domains are disoriented such that vector sum of the magnetizations is zero. When an external magnetic field is applied, the magnetization increase gradually and then rapidly, finally saturate at 131(emu/gm) which obtained at the magnetic field of 2.5 kOe , which is called saturation magnetization. In this point, the specimen becomes a single domain that is aligned in the direction of applied field. When H is reversed and reduced to zero, some magnetization remains, which is known as the remanence (B_r). This may be explained by the resistance to movement of domain walls, corresponding to the increase of H in the opposite direction. In order to remove the remanence, a reversed H is required. The field applied to reduce remanence to zero is called coercivity (H_c). Since all the domains have different magnetization direction, there is no magnetic flux ($B=0$) at point c. With increasing of field in the opposite direction, the same saturation happens as it did before. The cycle is then reversed to get a full hysteresis loop.

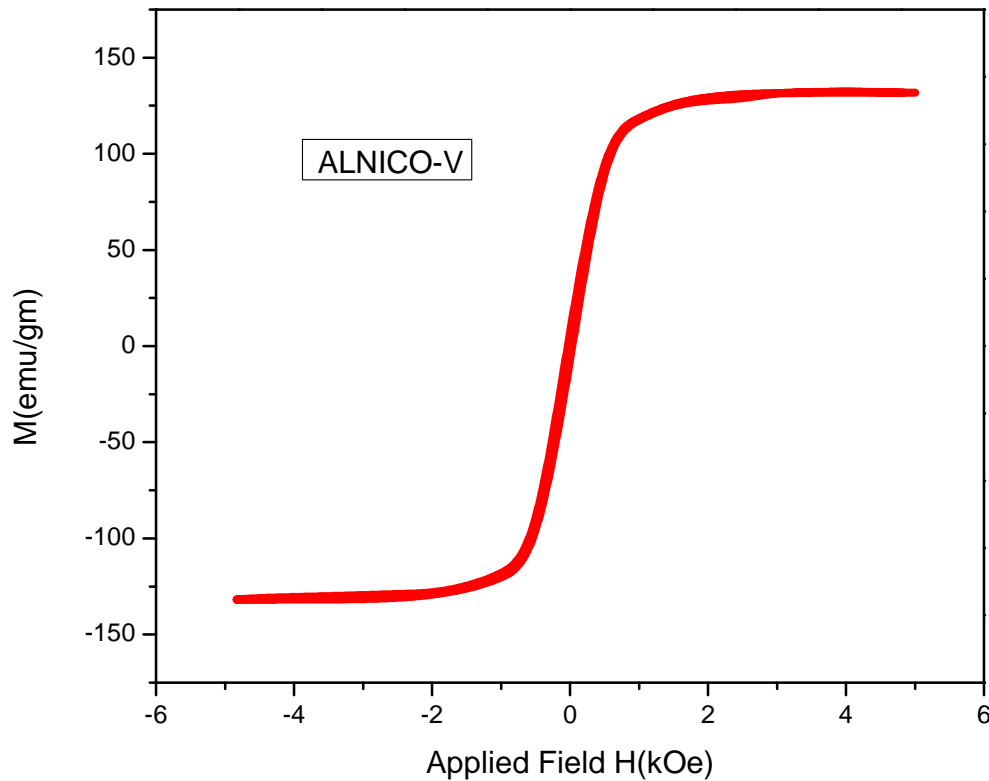


Figure 5.5 (a): M-H curve for Alnico v for room temperature

Fig 5.5 (a) shows the Alnico v permanent magnetic alloy is a soft magnetic material with low coercivity of 180 Oe at room temperature. The saturation magnetization is 131 emu/gm which is obtained at the applied magnetic field of 2.5 kOe. The low coercivity value indicates the small domain size of the material.

Coercivity Enhancement Heat Treatment

The ribbons were heat-treated under vacuum at temperatures 700-900 °C (for 2 - 30 minutes) and then were cooled to 600 °C with a cooling rate $\sim 4^{\circ}\text{C}/\text{min}$. The heat-treatment was continued at this temperature for 120 minutes. The as made M-H curve shows almost a line hysteresis

And the measured magnetization value is around 140 emu/gm.

The second M-H curve shows significant coercivity which is observed after annealing the ribbon at 900C for 30 minutes , and then cooling down to 600 C @4C/minute . The sample was then held at constant 600C for 4 hours and finally cooled down to room temperature.

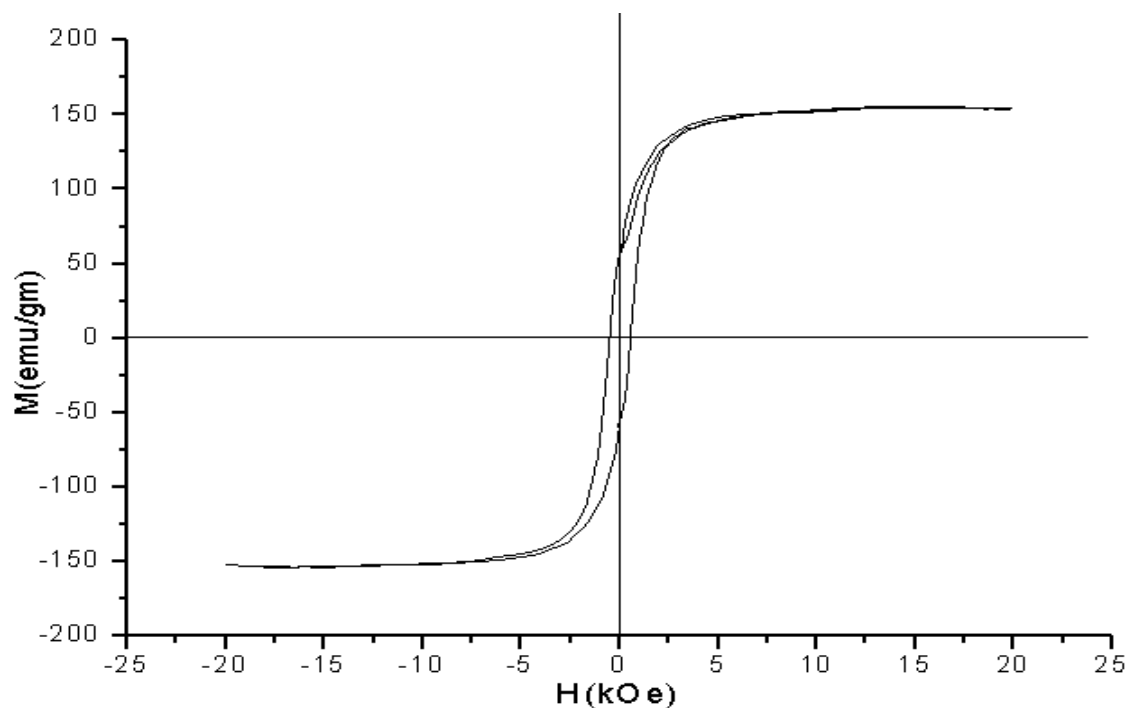


Figure 5.5 (b) : Hysteresis loops of Alnico V (900 °C for 30 minutes then 600 °C 4hours minutes ribbons.

The coercivities differ greatly between 180 and 1000 Oe for as made Alnico ribbon and annealing Alnico v ribbon respectively. To get a first estimate for the coercivity of Alnico a well-established relation for the coercivity of a fully aligned array of single domain particles is commonly used [5]

$$H_C = (1 - p)(N_z - N_x)M_S$$

Here p is the volume fraction of the *Fe Co*-rich α_1 -lamellae. $(N_z - N_x)$ denotes the difference in demagnetization factors between the principal directions of the lamella (i.e. the shape anisotropy contribution) and is the saturation magnetization of the α_1 - lamellae. M_S will increase with increasing content of Fe and Co, consequently the coercivity should be proportional to the Fe and Co concentration in the α_1 -phase. Since they are, within the error limits, almost the same for both samples we doubt that they are responsible for the relatively big difference in coercivity. However, the formula was derived for an ideal separation of the magnetic phases. This separation is regarded as a necessity for a high coercivity and therefore it is likely that the main reason for the decreased coercivity is the less defined chemical interface rather than the absolute change in composition. Similar conclusions were drawn by Xing et al. [9] in commercial Alnico 5-8 magnets and by Sun et al. [12]

5.6 Magnetoresistance Measurement

Magnetoresistance (MR) is a property of the materials to change its electrical resistance when magnetic field is applied. Magnetoresistance is defined as

$$MR\% = \frac{R(B) - R(0)}{R(0)} \times 100\% \quad (1)$$

Where $R(B)$ is the resistance in presence of magnetic field and $R(0)$ is the resistance in absence of magnetic field .

the resistivity of the material without magnetic field. At certain conditions anisotropy of the magnetoresistance appears in the manganese films. It can be described as the dependence of the magneto resistance on the direction of the magnetic field with respect to the direction of the current and the surface plane of the film. There are three main reasons for the anisotropy in the ferromagnetic materials: (1) the existence of the preferential directions of magnetization (due to the crystalline structure and deformations), (2) resistivity dependence on the angle between the direction of the current and the magnetization vector which is inherent in ferromagnetic materials and (3) the shape anisotropy of the sample (demagnetization effect). The main reason for the anisotropy in the ALNICO 5 crystalline manganese ribbon is due to the shape anisotropy [4]. MR of the magnates depends on the magnetic field inside the sample. In turn, the magnetic field inside material depends on the external magnetic field \mathbf{H}_{ext} and the demagnetizing field \mathbf{H}_d and can be calculated as: $\mathbf{H}_i = \mathbf{H}_{\text{ext}} + \mathbf{H}_d$. The demagnetizing field \mathbf{H}_d is proportional to the magnetization \mathbf{M} and the shape anisotropy tensor N : $\mathbf{H}_d = -N \cdot \mathbf{M}$. For this ribbon for \mathbf{M} normal to the surface the factor $N_x = N_y = 0$ and $N_z = 1$. Therefore, the preferred magnetization vector lies in the surface plane.

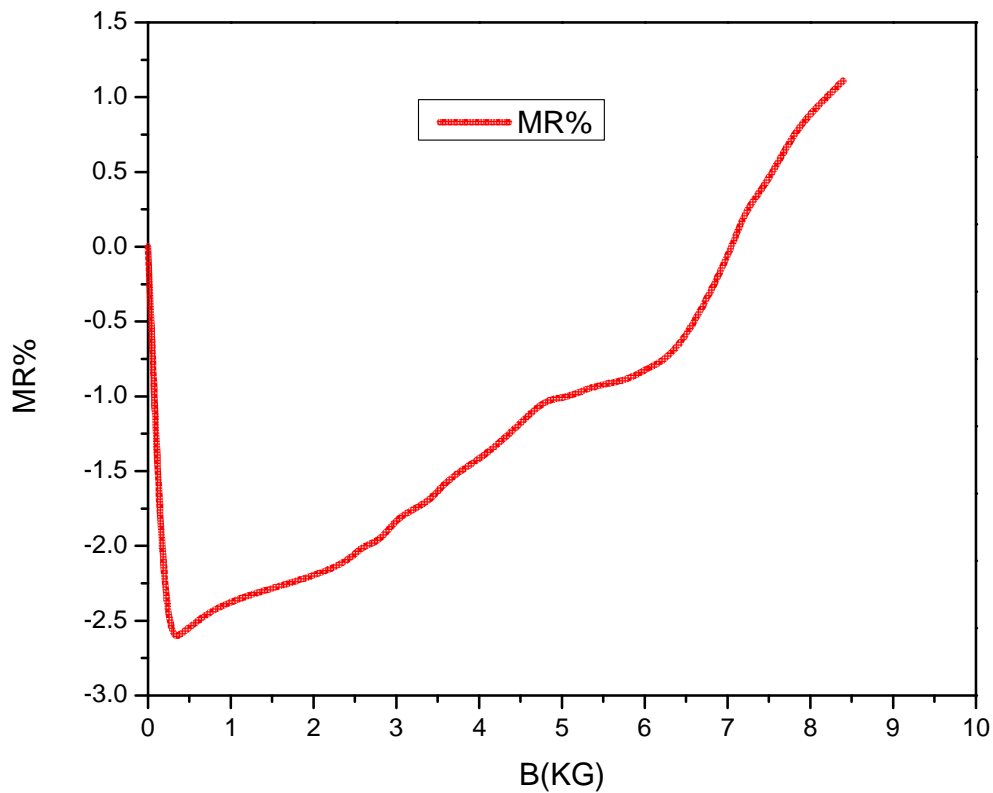


Fig.5.6 magneto resistance as function of magnetic field

The value of magneto resistance is found to vary from 0 to -2.59 % at the field 0.48 (KG). Magneto resistance is found to have decreased with applying field. when the applied field reached at more than 7 (KG) the value of magneto resistance is 0. Magneto resistance is also found to have increased with applying field. The value of magneto resistance is found to vary 0 to -2.59% at the field 0.48(KG) and 0 to 1.11% at the increasing field 7 to 8.4 (KG).

First we found the value of magneto resistance is negative this indicates that the materials are ferromagnetic and the positive portion indicates that it may be due to the magnetic disordering

process and is expected to have relatively weaker ferromagnetic coupling between ultra fine grains owing to the enhanced paramagnetic effect of V by the thermal agitation.

The fig 5.6 shows the behavior of magnetoresistive jump which means the alloy is shape memory. The physical mechanism behind this peculiar behavior is a martensitic transition (MT) from an ordered bcc toward a close-packed martensitic structure [6].

5.7 Study the temperature dependence of Resistivity of Alnico v (Four probe method)

Ohm's law: if physical conditions (like temperature mechanical stress) remains unchanged, then potential difference across the two ends of a conductor is proportional to current flowing through a conductor.

$$V \propto I \text{ or } V = IR.$$

The constant of proportionality, R is called resistance of the conductor.

The scalar equation $E = \rho J$ is only valid for resistors and conductors which are homogeneous and isotropic, that is the conductivity (reciprocal of resistivity) is uniform throughout the conductor, carrying a uniform electric current per unit cross-sectional area, J, through a uniform internal electric field E, all in one dimension only.

Four probe method

The 4-point probe set up (Fig.2) consists of four equally spaced tungsten metal tips with finite radius. Each tip is supported by springs on the end to minimize sample damage during

probing. The four metal tips are part of an auto-mechanical stage which travels up and down during measurements. A high impedance current source is used to supply current through the outer two probes, a voltmeter measures the voltage across the inner two probes to determine the sample resistivity. Typical probe spacings ~ 1 mm

These inner probes draw no current because of the high input impedance voltmeter in the circuit. Thus unwanted voltage drop ($I R$ drop) at point B and point C caused by contact resistance between probes and the sample is eliminated from the potential measurements

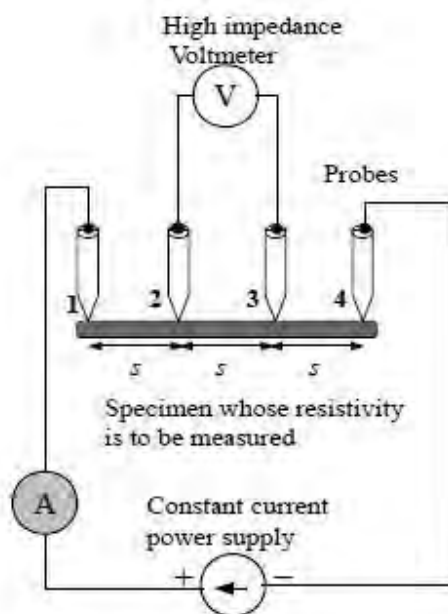


Fig.5.7 (a): Four probe method of a measuring resistivity of a specimen

Since these contact resistances are very sensitive to pressure and to surface condition (such as oxidation of either surface), error with the conventional two-electrode technique (in which potential-measuring contact passes a current) can be quite large.

The electric current carried through the two outer probes, sets up an electric field in the sample. In Fig.5.4, the electric field lines are drawn solid and the equipotential lines are

drawn broken. The two inner probes measure the potential difference between point B and C.

Resistivity measurement

The resistivity was measured by the four-probe method and using the following relation .At low temperature the resistivity

$$\rho = [\rho_o + \Delta\rho(T)] \exp [-2W(T)]$$

where ρ_o is the residual resistivity , $\Delta\rho(T)$ is the term arising from the inelastic electron – phonon interaction and the exponential term represents the Debye –Waller factor .the term , $\Delta\rho(T)$ is shown to exhibit $+T^2$ dependence at low temperature ($<200K$) + T at higher temperatures.

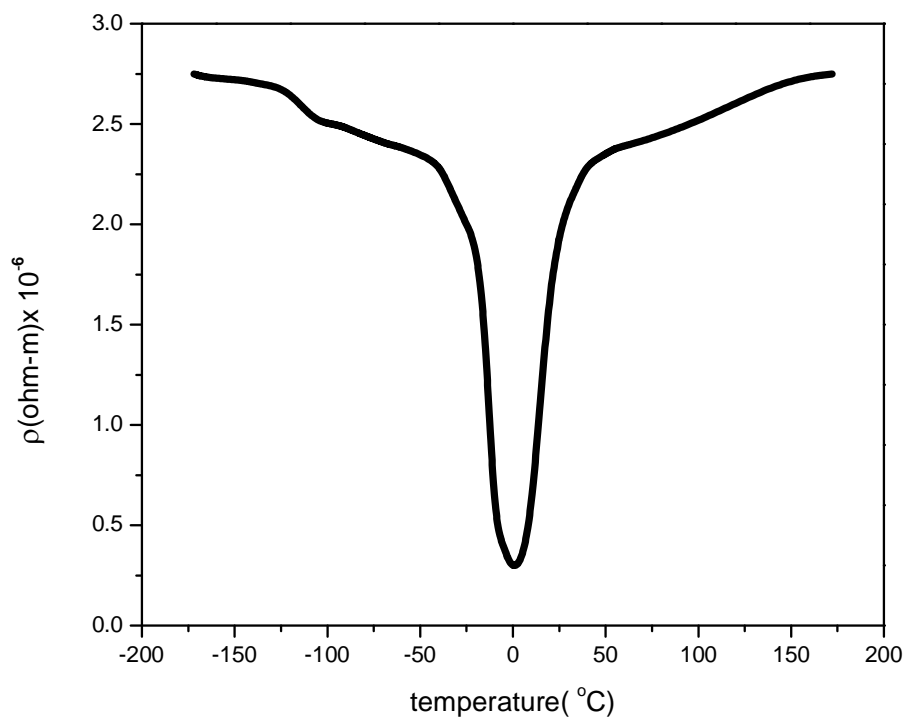
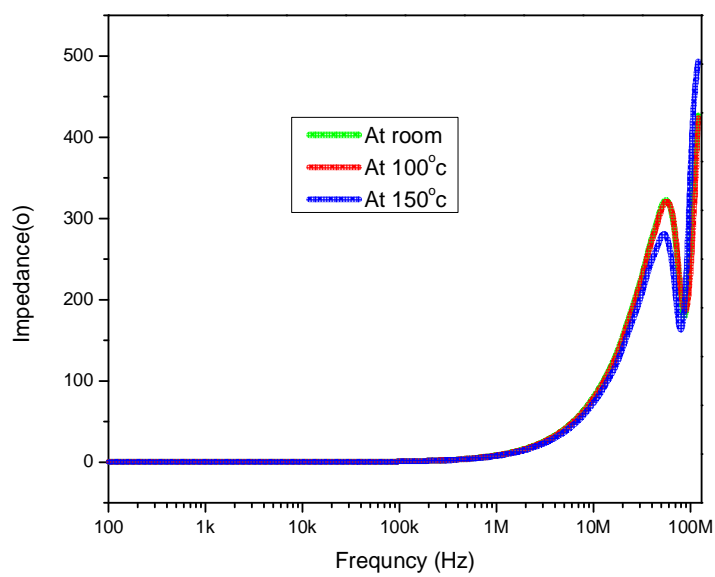


Fig.5.7 (b) : Resistivity as a function of temperature

The resistivity behavior is almost isotropic at -50°C to $+50^{\circ}\text{C}$ temperature going through a minimum at around 0°C .

5.8 Impedance and magnetic permeability versus frequency



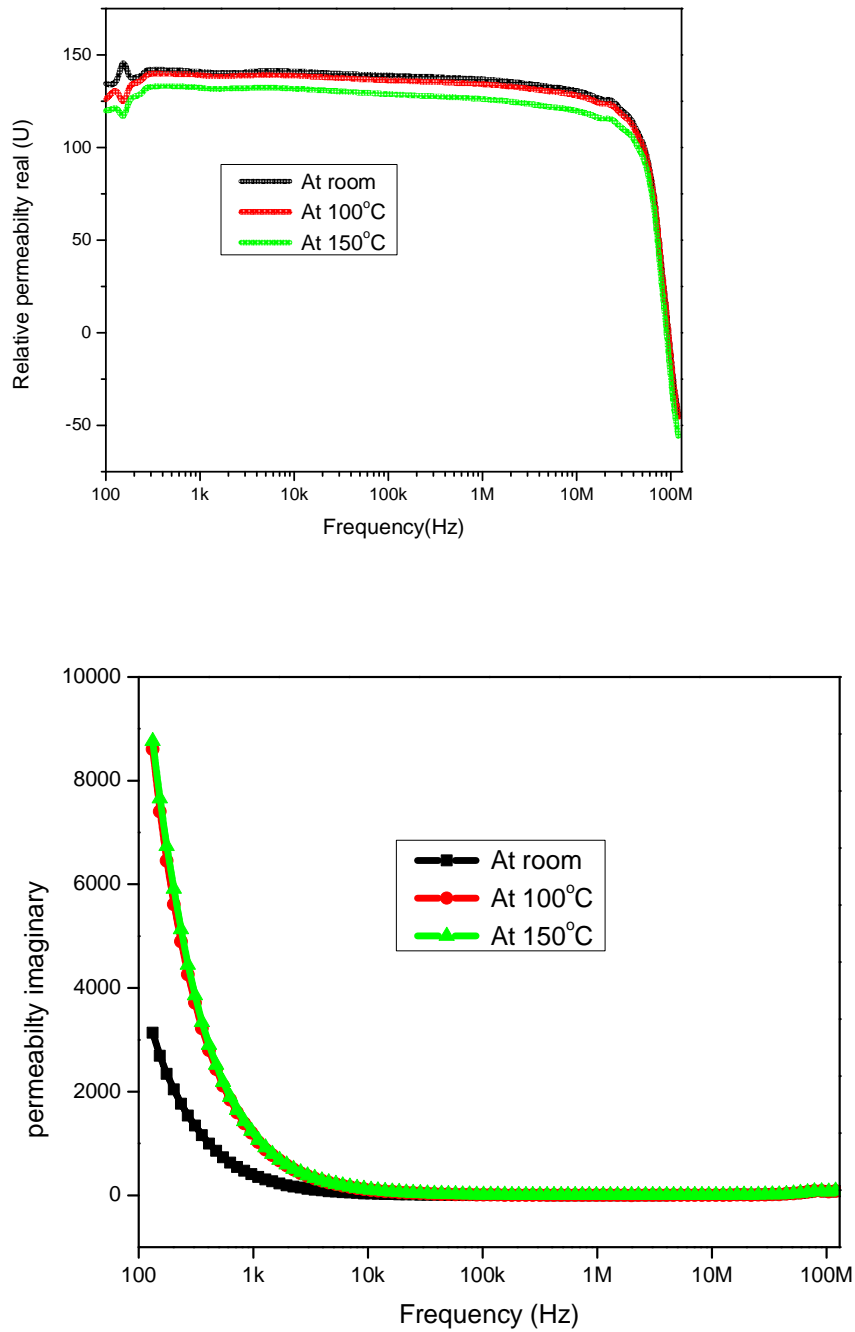


Fig 5.8 .alnico v ribbon form (a) frequency vs impedance at various temperature (b) frequency vs real part of permeability (c) frequency vs imaginary part of permeability

It can be seen the first fig (a) impedance as a function of frequency at a low frequency (100 Hz to 10 MHz) the alnico v ribbon at various temperature is low but when the frequency reaches at 10MHz the alnico ribbon is responded and increases impedance with increasing frequency .this behavior of this reasons is the sample is inductive with some anomaly at high frequency. But on the other hand at low frequency the alloy has no impedance with response of frequency. the sample 100 Hz to 10 MHz Figure 5.8(a) shows the corresponding trend in the impedance as a function of frequency. At low frequencies it is constant and equal to the DC value but increasing the frequency it is responded ac characteristics.

From the fig 5.8 (b) is observed the real permeability as a function of frequency with various temperature. at low frequency the sample is responded and is showed its resonance . Up to around 10 MHz the real permeability is steady and then drop with increasing frequency. At high frequency there is low permeability.

A good soft magnetic material should have minimal hysteresis and a high permeability. Permeability is usually quoted for the internal field, because soft magnets are normally used in a toroidal geometry where demagnetizing effects are negligible. In some range of internal field, the B(H) response is linear

$$B = \mu_0 \mu_r H$$

The frequency response of the permeability of high-frequency sample is flat up to the ferromagnetic resonance frequency, where it falls of. The higher the cut-of frequency, the lower the permeability.

Besides the fig 5.8 (c) shows imaginary part of permeability .It is seen from the figure at low frequency the imaginary permeability also high and at room temperature at 1kHz the permeability drop. That is indicated inversely relation real and imaginary permeability.

The whole phenomena can be explained as below. Here, we focus on the magnetization dynamics of coherent precession (MDCP), which is related to higher permeability at higher working frequencies of high frequency magnetic materials (HFMM).

HFMM are considered as the magnetic materials with high permeability $\mu(\omega)$ and small loss of energy at high working frequencies ω . The higher permeability means a bigger response of the magnetic density $B = \mu(\omega)H$ to an applied magnetic field H , and the lower loss of energy means a more efficient driven effect of H . Certainly, both permeability and loss of energy are closely related to the dynamics of magnetization M , that is, the dynamic process of magnetization under an applied magnetic field H . Below kHz, the main dynamic processes of magnetization are coherent rotation and the displacement of the domain wall[7]which is quite similar to the static situation. Consequently, the permeability $\mu = B/H$ is almost constant, where B is determined by M . Therefore, soft magnetic materials with high saturation magnetization M_s are always the best choice. As the eddy loss can be depressed by decreasing the size or thickness and/or increasing the resistivity of the magnetic materials, Beyond the 1 GHz range, besides the eddy loss, the significant challenge is to find materials with high permeability. Since the permeability of bulk magnetic materials is mainly determined by magneto crystalline anisotropy, it is quite difficult to obtain bulk magnetic materials with permeability larger than 20 at the GHz range. Magnetic nonmaterial's, such as nanoparticles, nanowires, and thin films, seem to be potential candidates for HFMMs. It has been found that spherical particles, nanowires, and their composites cannot reach the target, for either ferrites or metallic alloys.[12] However, in quasi two-dimensional

systems, such as thin films[14] and flake particles,[13] high permeability in the GHz range has been realized, even if the composition is the same as that of the bulk materials.

The key high frequency magnetic property in GHz range, the frequency dependence of permeability, is determined by the MDCP, which is described by the LLG equation. For a ferromagnetic system, if we know its density of free anisotropy energy F , the effective magnetic field $H_{\text{eff}} = -\frac{1}{\mu_0} \nabla F$, the frequency dependence of permeability can be obtained. Generally, higher resonance frequency means higher working frequency, and higher initial rotational susceptibility means higher working permeability. Therefore, the high frequency magnetic properties of magnetic materials can be represented as the product of the initial rotational susceptibility and the resonance frequency. It is known that the initial rotational permeability μ_i is the sum of susceptibility χ and 1. Historically, several important simple models show clearly the relationship of the initial rotational permeability and the resonance frequency with the saturation magnetization and the anisotropy field. This relationship points out the ways to improve the high frequency magnetic properties and to find new HFMM. In the following, we summarize the results of these important models by solving the LLG equation without the damping.

Snoek's limit and planar ferrite consider the simplest ferromagnet, a single domain spherical crystal with a uniaxial magneto crystalline anisotropy. The density of the anisotropy energy is

$F = K_0 + K_1 \sin^2 \theta$, where K_0 and K_1 are anisotropy constants, and θ is the polar angle away from the easy axis. By using Eq. (5), the effective anisotropy field can be written as $H_{\text{eff}} = \frac{2K_1}{\mu_0 M_s} \cos \theta$. (7) For a small angle precession, $\theta \rightarrow 0$, $H_{\text{eff}} = H_K = \frac{2K_1}{\mu_0 M_s}$ is constant. From the LLG equation (4) without damping, the product of the initial rotational permeability μ_i and

the resonance frequency f_r satisfies $(\mu_i - 1)f_r = \gamma 2\pi M_s$, (8) where $\mu_i = 1 + M_s/HK$, and $f_r = \gamma HK$. If the sample is composed of a series of single domain spherical crystals without interaction, supposing a randomly distributed anisotropic field, the famous Snoek's law[16,17] can be obtained $\chi_i f_r = (\mu_i - 1)f_r = \gamma 3 M_s$. (9) It is found that the product of the initial rotational susceptibility and the resonance frequency is proportional to the saturation magnetization. This means that the only way to seek better high frequency magnetic materials is to fabricate materials with higher saturation magnetization. Compared to Snoek's law, in addition to the saturation magnetization, the anisotropy field has a strong effect on the high frequency properties. However, to change the magneto crystalline anisotropy field of a crystal, we have to change the symmetry of the crystalline field and/or the content and distribution of elements in the magnetic materials. This implies the same difficulty as Snoek's law when searching for different magnetic materials with better high frequency properties.

5.9 compare with impedance and permeability at room temperature ribbon and powder form.

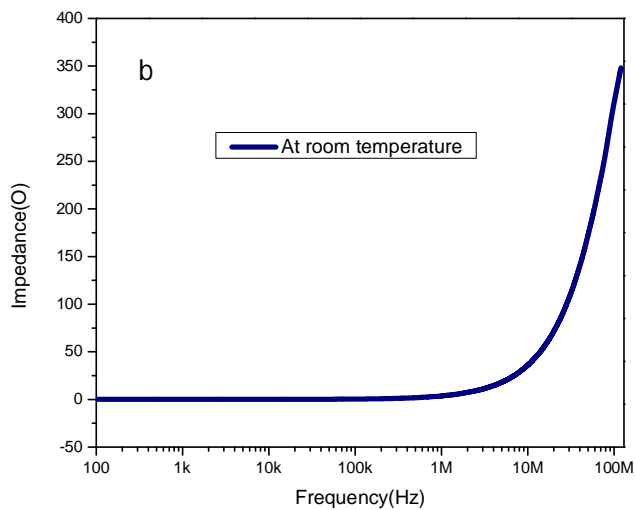
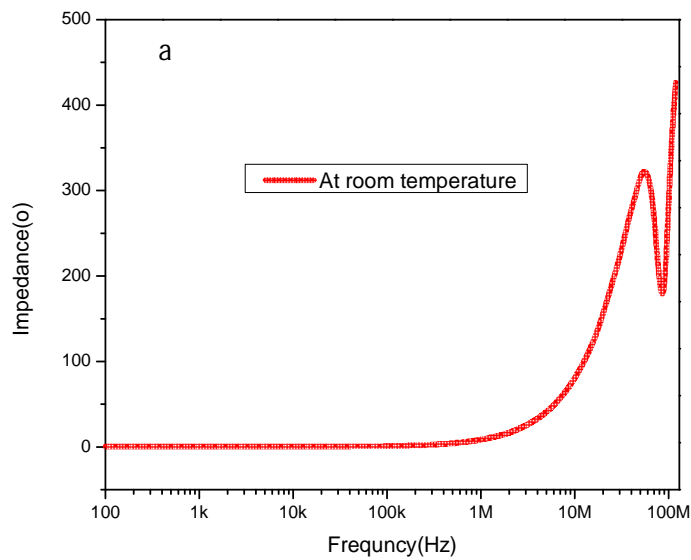


Fig.5.9 : frequency vs impedance at room temperature with (a) ribbon form (b) powder form

At room temperature impedance of ribbon remains steady 100Hz to 10 MHz and we found anomaly at 10MHz 100 MHz but on the other hand the powder form of alnico 5 ribbon steady from 100Hz to 10MHz and then it rapidly increase without anomaly.

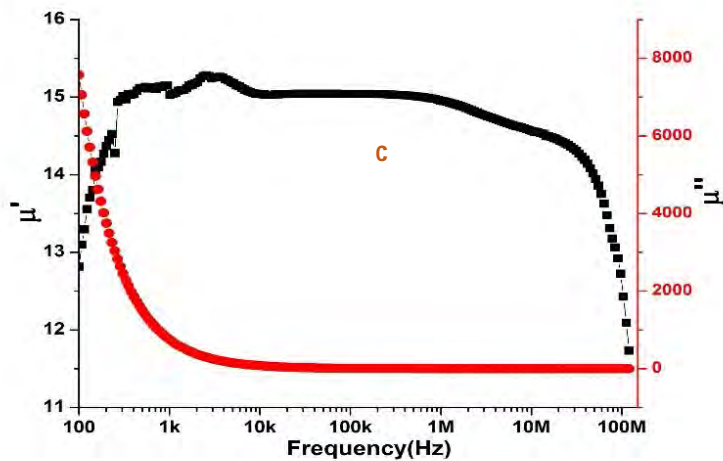


Fig.5.9 (c) : real permeability and imaginary permeability vs frequency of powder form.

It is also observed from the fig5.9 (c) the powder form of ribbon real part and imaginary part of permeability with respect to frequency. The real part of permeability at low temperature we find some disturbance of its resonance and then its drop with increasing frequency. The imaginary permeability is the same as before.

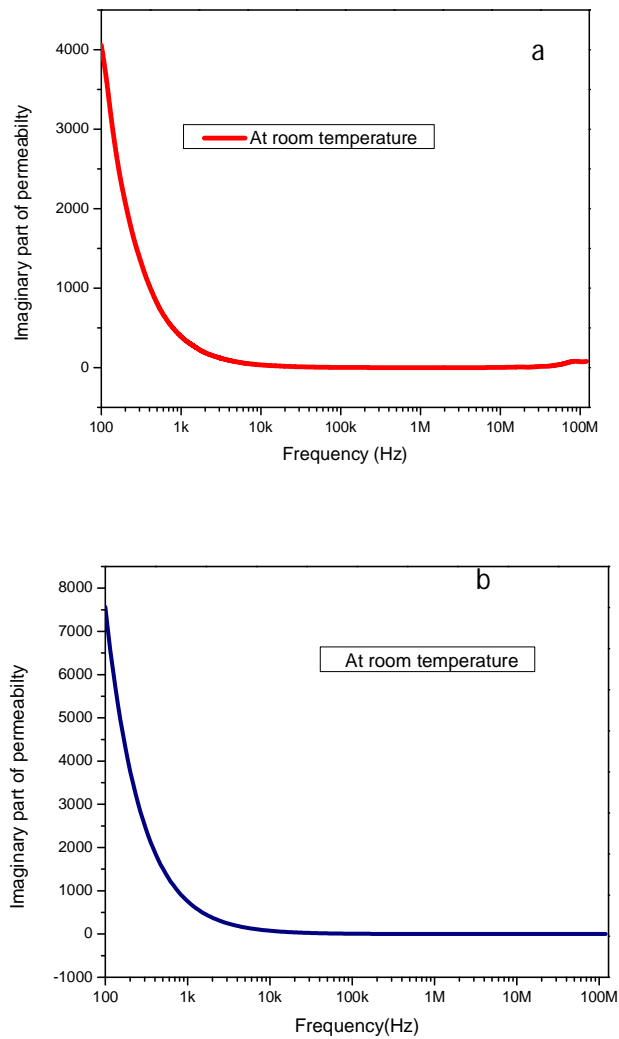


Fig.5.10 (d) frequency vs imaginary permeability at room temperature with ribbon form and powder form .

The fig 5.10 (d) shows there are no difference as made sample and powder form of permeability. That means the loss part of permeability is same as before.

References:

- [1] O Akdogan, L Wanfeng, and G Hadjipanayis, *J Nanopart Res*, no. 14, p. 891, 2012.
- [2] M J Kramer, R W McCallum, I A Anderson, and S Constantinides, *JOM*, no. 64, p. 752, 2012.
- [3] O Gutfleisch et al., *Adv. Mater.*, no. 23, p. 821, 2011.
- [4] M D Kuz'min, K P Skokov, H Jian, I Radulov, and O Gutfleisch, *J Phys: Cond Mat*, no. 26, p. 064205.
- [5] T Mishima, *Stahl U. Eisen*, no. 53, p. 79, 1931.
- [6] R A McCurrie, *Structure and Properties of Alnico Permanent Magnet Alloys*. In E.P Wolfarth (Ed.) *Ferromagnetic Materials 3*. UK: North-Holland Publishing Company, 1982.
- [7] L Zhou et al., *Metall. Mater. Trans.*, no. E1, p. 27, 2014.
- [8] L Zhou et al., *Acta Mater*, no. 74, 2014.
- [9] Y L Sun et al., *J. Magn. Magn. Mater.*, no. 379, p. 58, 2014.
- [10] Q Xing et al., *IEEE Trans. Magn.*, no. 49, p. 3314, 2013.
- [11] T A Abinandanan and H Ramanarayan, *Bull. Mater. Sci.*, no. 26, p. 189, 2003.
- [12] O Akdogan, L Wanfeng, and G Hadjipanayis, *J Nanopart Res*, no. 14, p. 891, 2012.
- [13] X Y Sun et al., *J. Magn. Magn. Mater.*, no. 348, p. 27, 2013.
- [14] Sohn J, Han S H, Yamaguchi M and Lim S H *Appl. Phys. Lett.* 89 103501,2006
- [15] Sun Z Z and Wang X R *Phys. Rev. Lett.* 97 077205,2006
- [16] Sukhov A and Berakdar J *Phys. Rev. Lett.* 102 057204,2009
- [17] Bloch F *Z. Phys.* 61 206,1930

Chapter Six

6.1 CONCLUSION

we have found that in ribbon form of alnico 5 retain crystalline structure that is unconventional to compare other glassy material. All the as made and annealed samples have shown pure crystalline structure as revealed by the X-ray Diffraction analysis unlike most of the iron, cobalt and nickel based ribbons which show amorphous or glassy structure after melt-spinning.

Ribbons fabricated at different wheel speeds (25 m/s – 50 m/s) have been studied for their thermal , structural and magnetic properties. The effect of wheel speed on the magnetic properties have been investigated. It is found that change in wheel speed has an effect on the ductility of the ribbons.

It is observed through this studies that aging the ribbons at high temperature has a positive effect on the coercivity enhancement of the ribbons. The as made ribbons have a relatively low coercivity and only a uniaxial anisotropy which is induced due to mechanical stress during the growth process is present. However annealing at high temperature followed by aging has yielded a significant increase in coercivity.

The magneto resistance behavior is found to be typical in nature and has shown a minimum around 1 kOe which is also near the coercive field obtained after Alnico regular heat treatment followed by aging

6.2 Suggestions for Further Work

We will further investigate the material alnico 5 alloy to understand the thermo magnetic behavior at high temperature where the alloys are still magnetic. The origin of coercivity will also be investigated in the light of spinodal decompositions. The sample will be governed at different rpm for different time to investigate the microstructure of this alloy .It is expected that grain size of alloy will be transform to even few tens of nanometer but still above the super paramagnetic limit.

Several of the hypotheses presented here could be more thoroughly investigated to develop a better understanding of the thermodynamics and kinetics of the alnico system, particularly in regards to the γ and σ phases. A time-temperature-transformation study of the γ phase should be completed. Effects of oxides and impurities, cooling and heating rates, grain size, decomposition of α , and local homogeneity of the starting material will need to be considered.

Further analysis of the gas-atomized powders should be pursued to determine what size ranges of powders exhibit cell boundaries with ADZ, and if any other composition fluctuations exist. Low temperature annealing effects on powders with ADZ should be conducted to see if the fluctuations are removed.